Tectonophysics 817 (2021) 229029

Contents lists available at ScienceDirect

Tectonophysics

journal homepage: www.elsevier.com/locate/tecto

# The peridotite deformation cycle in cratons and the deep impact of subduction

Emily J. Chin [a,*], Benjamin Chilson-Parks [b,c], Yuval Boneh [d], Greg Hirth [b], Alberto E. Saal [b], B. Carter Hearn [e], Erik H. Hauri [f]

[a] Scripps Institution of Oceanography, University of California San Diego, 9500 Gilman Drive, La Jolla, CA 92093, USA
[b] Department of Earth, Environmental, and Planetary Sciences, Brown University, 324 Brook Street, Providence, RI 02912, USA
[c] Department of Geosciences, University of Connecticut, 354 Mansfield Road - Unit 1045, Storrs, CT 06269, USA
[d] Geological and Environmental Sciences, Ben-Gurion University of the Negev, Mailbox 653, Beer-Sheva, Israel 84105
[e] MacLean, Virginia, USA
[f] Earth & Planets Laboratory, Carnegie Science, Washington DC 20015, USA

ARTICLE INFO

*Keywords:*
Xenolith
Craton
EBSD
Water

ABSTRACT

Xenoliths play a crucial role in interpretation of mantle deformation and geochemistry. The classic work of Mercier and Nicolas (1975) introduced the concept of the peridotite deformation cycle, which connected observed microstructures to a physical sequence of deformation. We revisit Mercier and Nicolas' original concept, bringing in new constraints using large area EBSD maps and associated microstructural datasets, analysis of water contents in nominally anhydrous minerals, and trace element chemistry of pyroxenes and garnets. We apply these techniques to a well-characterized suite of peridotite xenoliths from the Eocene-age Homestead and Williams kimberlites in the northwestern Wyoming Craton. Pyroxene water content and trace element mineral chemistries reveal ubiquitous hydrous metasomatism beneath the craton, most likely linked to the Cenozoic Laramide Orogeny. Homestead xenoliths primarily exhibit coarse protogranular and equigranular textures, B-type olivine fabrics, and generally elevated mineral water contents compared to Williams. Xenoliths from Williams are strongly deformed, with porphyroclastic and transitional textures containing annealed olivine tablets, mostly A-type olivine fabrics, and generally lower mineral water contents. As a whole, mantle from Homestead to Williams reflects a cratonic scale deformation cycle that likely initiated in Laramide times and lasted until the end of orogeny in the Eocene. At Williams, evidence for a rapid deformation "sub-cycle" within the main deformation cycle is preserved in the tablet-bearing xenoliths, corresponding to the enigmatic "transitional" texture of Mercier and Nicolas (1975). Our results suggest that this texture reflects interruption of the main deformation cycle by processes possibly related to a rapidly forming lithospheric instability and generation of the kimberlite magma – offering a new interpretation of this ambiguous peridotite texture. Collectively, our results incorporate typically disparate geochemical and textural datasets on xenoliths to shed new insights into how metasomatism, volatiles, and deformation are connected in the deep cratonic lithosphere.

## 1. Introduction

Information about deformation in the Earth's mantle comes from regional to global observations of seismic anisotropy (Long and Becker, 2010) coupled with investigation of the fabrics of mantle rocks erupted as xenoliths and exhumed as massifs (Ave'Lallemant and Carter, 1970; Basu, 1977; Nicolas et al., 1980; Tommasi et al., 2004; Baptiste et al., 2012). Linking these two datasets is not always straightforward because deformation textures in the olivine-dominated mantle, expressed as crystallographic preferred orientation (CPO), depend on several factors that reflect the integrated result of tectonic and geochemical events. Factors that may affect olivine CPO include water content (Jung and Karato, 2001), presence of melt (Holtzman et al., 2003; Le Roux et al., 2008), geometry of deformation (Tommasi et al., 1999; Bernard et al., 2019), inherited texture (Boneh and Skemer, 2014; Boneh et al., 2015), as well as pressure and temperature (Karato et al., 2008; Mainprice et al., 2005).

* Corresponding author.
*E-mail address:* e8chin@ucsd.edu (E.J. Chin).

https://doi.org/10.1016/j.tecto.2021.229029
Received 5 February 2021; Received in revised form 28 July 2021; Accepted 11 August 2021
Available online 14 August 2021

In certain regions of Earth, such as beneath cratons, the mantle lithosphere has survived for billions of years, and yet reveals complex internal structure that remains poorly understood (Silver, 1996). The antiquity of cratonic lithospheric mantle derives from a unique stability imparted through large extents of melt depletion (chemical buoyancy) that counteracts the negative thermal buoyancy of a thick, old, and cold keel (Jordan, 1981). Xenoliths erupted throughout Earth history (Heaman et al., 2019) indicate that cratons experience significant chemical modification (Foley, 2008; Menzies and Hawkesworth, 1986), which, together with large scale tectonic deformation, may eventually lead to craton de-stabilization (Dave and Li, 2016; Wu et al., 2019). While a craton's current state of demise may be inferred from seismic structure, velocity, and geodynamic models, the actual sequence of events leading up to destabilization can potentially be understood by unraveling the complex microstructural and geochemical signatures recorded in xenoliths.

### 1.1. From xenoliths to tectonics

Xenoliths represent occasional and fragmentary Rosetta Stones to unlocking the history of the lithospheric mantle. Because of their temporal and spatial limitations, it is crucial to extract as much microstructural, geochemical, and isotopic information from xenoliths as possible, preferably from the same specimens within a given xenolith suite to yield internally consistent datasets. Xenoliths have long been studied for their geochemical and isotopic compositions, resulting in canonical models of the upper mantle composition (e.g., McDonough and Sun, 1995). Regarding microstructure, the first, and foundational, strategy of xenolith classification was proposed by Mercier and Nicolas (1975) and Boullier and Nicolas (1975). These two papers produced a comprehensive petrofabric analysis of hundreds of peridotite xenoliths from around the world (both off-craton and craton), distilled into a framework for understanding texture as a product of deformation (Figs. 1, 2). Mercier and Nicolas (1975) also established the descriptive nomenclature for peridotite textures (Fig. 2) that mantle petrologists continue to use. The papers of Mercier and Nicolas (1975) and Boullier and Nicolas (1975) were the first steps allowing petrologists, structural geologists, and global seismologists to come together as a coherent community and infer mantle tectonics extrapolated from individual xenolith CPO and microstructures. Following the 1975 papers, subsequent refinements to the original textural nomenclature were published by Harte (1977) and Pike and Schwarzman (1977). However, the conceptual underpinning of the deformation cycle remained. Numerous regionally focused xenolith studies inspired by Nicolas' pioneering work also began to link geochemistry to texture (Basu, 1977; Downes, 1987; Embey-Isztin, 1984; Francis, 1978; Helmstaedt et al., 1972; Ross, 1983; Seyler and Mattson, 1989). These studies were instrumental in developing our modern understanding of the state of stress, deformation, and its implications for textural and compositional heterogeneities in the deep continental lithosphere (Carter and Tsenn, 1987; Karato, 2010; Mercier, 1980; Baptiste et al., 2012).

In the following decades, high-pressure, high-temperature rock deformation experiments have been added to the tools of observations, which connected the geometry of deformation to the formation of olivine CPO and then back to observations of seismic anisotropy (Nicolas et al., 1973; Zhang and Karato, 1995; Karato et al., 2008; Skemer and Hansen, 2016; Tommasi et al., 1999; Tommasi et al., 2009).

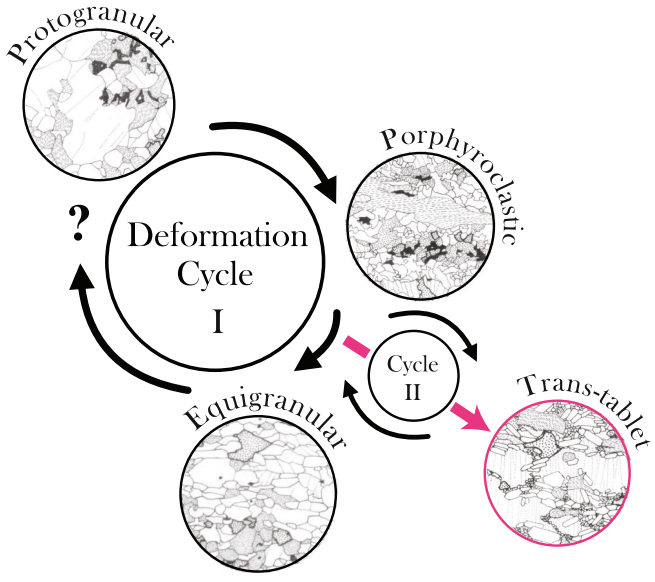


**Fig. 1.** Schematic diagram illustrating the original peridotite deformation cycle (I) of Mercier and Nicolas (1975) with their original line illustrations. Blank = olivine (dotted lines represent subgrain boundaries), dashes = orthopyroxene, heavy dots with heavy contours = clinopyroxene, black infill = spinel. A second cycle (Cycle II) is proposed to represent the "transitional" texture of Mercier and Nicolas (1975).

### 1.2. The peridotite deformation cycle

A central concept of Mercier and Nicolas (1975) was the idea of the "deformation cycle" (Fig. 1), which linked observed textures (Fig. 2) to a generalized, chronological sequence of deformation events in mantle peridotite. Prior to lithospheric deformation, peridotites are inferred to have a protogranular texture, exemplified by coarse grain size (sometimes with olivine >1 cm) and olivine curvilinear grain boundaries (Figs. 1, 2a). The protogranular texture may reflect a metamorphic process associated with recrystallization coeval with peridotite melt depletion, forming the characteristic curvilinear grain boundaries (Mercier and Nicolas, 1975). With increasing deformation, the rocks evolve to porphyroclastic texture, with a recrystallized, fine grained olivine matrix, porphyroclasts of pyroxene, and a strong olivine CPO (Fig. 1, 2b, c). A sub-type of porphyroclastic texture, called "transitional" (Fig. 2c), was also identified by Mercier and Nicolas (1975). The transitional texture was interpreted to represent intermediate development from a strongly porphyroclastic texture to a final, equigranular or tabular equigranular texture (Fig. 2d). The transitional texture is identified by the presence of strain-free, straight-lined olivine tablets superimposed on a pre-existing porphyroclastic texture (Boullier and Nicolas, 1975). The tablets are sometimes observed to "grow" into large, internally deformed porphyroclasts (Fig. 1, 2c; Drury and Roermund, 1989 and Fig. 8 therein). The completion of the deformation cycle is marked by the evolution of porphyroclastic/transitional textures to fully recrystallized and recovered with characteristics of well-developed 120° triple grain-junctions. These textures are denoted as equigranular (Fig. 2d) and coarse tabular (Fig. 2d). Though the latter contains tabular olivine, it is distinguished from transitional texture in that the tabular grains have clear evidence of internal deformation microstructures such as subgrains and undulose extinction (Fig. 2d). By contrast, olivine tablets of the transitional texture lack internal deformation microstructure (cf. Boullier and Nicolas, 1975).

### 1.3. The transitional-tablet texture

The transitional textured peridotites have posed an enigma to mantle petrologists. The formation of olivine tablets has been ascribed to annealing in the presence of a grain-boundary fluid, linked to both deformation and fluid infiltration associated with kimberlite ascent (Drury and Roermund, 1989; Falus et al., 2004; Arndt et al., 2010). However, thermobarometry and olivine water content of transitional textured peridotites from the Wyoming Craton together with similar microstructures induced by post-deformation annealing experiments indicates that annealing at high homologous temperatures under dry

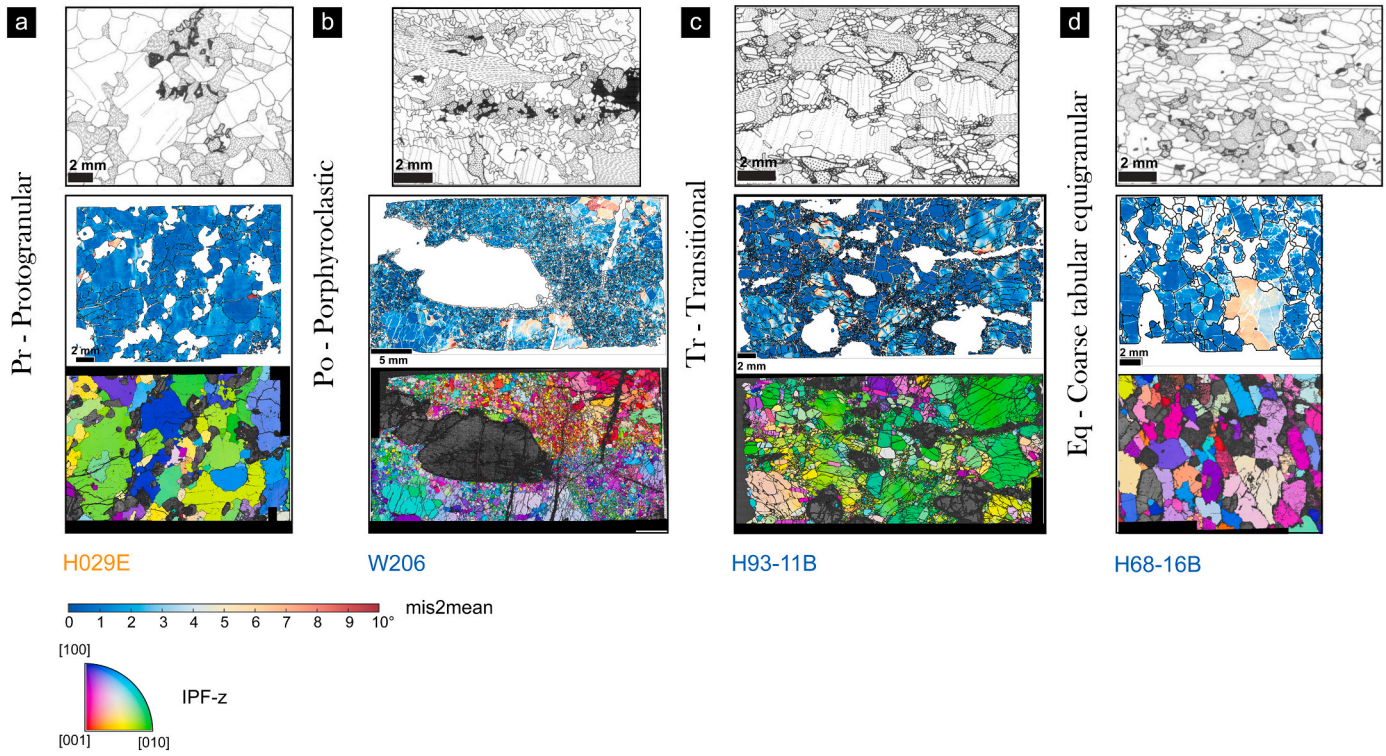


**Fig. 2.** Top row: original line drawings from Mercier and Nicolas (1975) illustrating the textural progression of the peridotite deformation cycle. See Fig. 1 caption for legend. a) Protogranular, b) Porphyroclastic, c) Transitional, d) Equigranular. Middle row: representative examples from the Homestead and Williams xenolith suite showing analogous textures to the original definitions. Maps shown are olivine mis2mean, where olivine grains (a grain is defined by a misorientation angle >10°) are colored in blue (low internal misorientation) to red hues (high internal misorientation). White areas represent other phases (garnet, pyroxenes) not included in this mis2mean analysis. Bottom row: Olivine orientation maps colored by the IPF (inverse pole figure) in the z sample direction of the representative Homestead and Williams xenoliths. Color key shows the distribution of crystallographic axes in the sample reference frame. Non-olivine phases (pyroxenes, garnet) are shown as band contrast (gray hues).

conditions could also be conducive to tablet formation (Boneh et al., 2021; Boneh et al., 2017). In the scenario proposed by Boneh et al. (2021), kimberlite fluids are not necessary to induce tablet growth, and estimates of annealing rates indicate that the tablets formed on timescales significantly longer than that of the kimberlite eruption.

Transitional textured xenoliths with tablets (or transitional-tablet, as we refer to it henceforth) are most commonly found in cratonic kimberlite-hosted xenoliths. The following list is by no means exhaustive, but highlights some well-known examples. Kimberlite-borne, transitional-tablet peridotite xenoliths are found in South Africa (Mercier and Nicolas, 1975; Boullier and Nicolas, 1975; Harte et al., 1975; Drury and Roermund, 1989; Arndt et al., 2010; Baptiste et al., 2012), Greenland (Arndt et al., 2010), Canada (Arndt et al., 2010), and northwestern Montana (Hearn and McGee, 1984). Tablet-bearing xenoliths are also found off-craton, with one well-studied example from Hungary (Falus et al., 2004). Although comprehensive field counts are limited, a survey of mine dumps at Jagersfontein, South Africa found that 33% of the observed xenoliths ($n = 133$) were porphyroclastic and/or "mosaic" textured – these include the transitional texture as well as highly strained, "fluidal" and mylonitic textures (Boullier and Nicolas, 1975). Furthermore, the comprehensive microstructural study of South African xenoliths by Baptiste et al., 2012 also corroborated a high percentage (~50%) of porphyroclastic and mylonitic peridotites at Jagersfontein (it is unclear whether the Baptiste et al. survey included transitional textures, as this texture is often considered a type of porphyroclastic). At the nearby Kimberley mine, 60% of the xenoliths analyzed by Baptiste et al. (2012) were also porphyroclastic/mylonitic.

The characteristic feature of transitional-tablet texture is that strain-free tablets overprint a pre-existing, highly deformed porphyroclastic texture. The stored strain energy that provides the driving force responsible for tablet formation was previously acquired during a high-temperature deformation event in the lithospheric mantle which produced the initial porphyroclastic to mylonitic fabric. Thus, the transitional-tablet texture represents a "sub-cycle", or interruption, within the main deformation cycle (e.g., Harte et al., 1975) (Fig. 1).

It is unclear what could promote deformation events that generate the pre-cursor pophyroclastic/mylonitic texture. A geologically recent example of extremely mylonitized, highly strained xenoliths found at Lunar Crater, Nevada (Dygert et al., 2019), was hypothesized to represent microstructures that formed during a lithospheric "drip" beneath the Great Basin (West et al., 2009). In the case of the Cretaceous South African kimberlites, the Jagersfontein and Kimberley kimberlites (which both contain abundant porphyroclastic and transitional-tablet xenoliths) erupted close to a major intracratonic suture (the Colesberg Lineament), whereas Premier, Finsch, and Monastery kimberlites (which contain fewer highly deformed xenoliths) are further from major sutures (Field et al., 2008). Within the Wyoming Craton (Fig. 3), xenoliths erupted closer to the craton interior at the Homestead kimberlite contain only ~5% porphyroclastic textured peridotites (Hearn, 2004), whereas xenoliths erupted closer to the craton edge at the Williams kimberlite, near the Great Falls suture zone, contain abundant porphyroclastic and highly deformed textures (Hearn and McGee, 1984). It has long been proposed that kimberlites exploit lineaments, either relict features from tectonism during craton coalescence (Jelsma et al., 2004; Watterson, 1975), or more recent features associated with craton margin

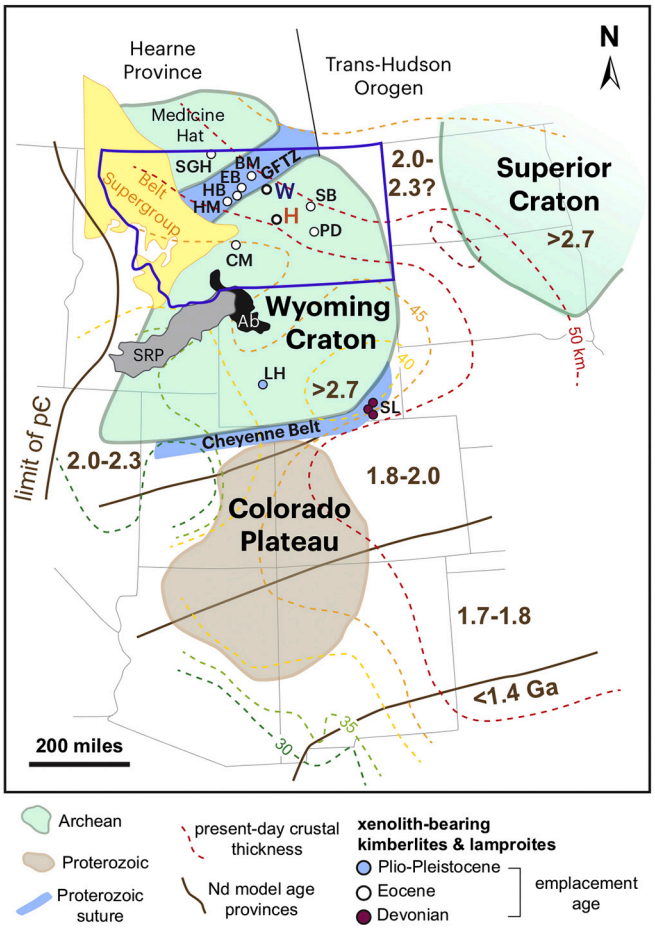


**Fig. 3.** Map of the Western USA showing Wyoming and Superior Cratons and Colorado Plateau. Filled colored and white circles represent kimberlites, lamproites, and similar volcanic rocks that erupted xenoliths. SRP = Snake River Plain (Miocene to present). AB = Absaroka volcanism (Eocene). Dashed lines represent contours of present-day constant crustal thickness from Bird (1984). Much of the crust <40 km may have resulted from Neogene Basin and Range extension; thickened crust >40 km is the result of Laramide basement cored uplifts. Numbers in brown text are Nd model age provinces from Bennett and DePaolo (1987). HM, Highwood Mountains; SGH, Sweetgrass Hills; BM, Bearpaw Mountains; EB, Eagle Buttes; HB, Haystack Butte; W, Williams (located in the Missouri Breaks diatremes); H, Homestead; SB, Smoky Butte; PD, Porcupine Dome; CM, Crazy Mountains; LH, Leucite Hills; SL, State Line. pC, Precambrian. Belt Supergroup represents thick sedimentary sequences deposited ca. 1.47–1.40 Ga on Archean and Paleoproterozoic crystalline basement.

reactivation owing to far-field stresses induced on cratonic lithosphere from rifting or subduction (Stracke et al., 1982; Tappe et al., 2018; Duke et al., 2014). Interestingly, the transitional-textured xenoliths from the Pannonian Basin were erupted in alkali basalts thought to be related to slab rollback during the middle Miocene (Falus et al., 2004).

The objective of this study is to refine the original concept of the peridotite deformation cycle with a new interpretation of the poorly studied transitional-tablet texture. To this end, we investigate a suite of kimberlite-hosted peridotite xenoliths from the Wyoming Craton. We show that olivine fabric, water content, and clinopyroxene and garnet trace element geochemistry vary with the conventional textural types of the background main deformation cycle, and that the transitional-tablet texture represents rapid recovery from short-lived, high strain events in the lithosphere, followed by immediate capture and preservation in the volcanic host.

## 2. Geologic background

The Wyoming Craton (Fig. 3), alongside part of the Superior Craton, form the southern terminus of Laurentia, a collective of Archean cratons and Proterozoic terranes (Bleeker, 2003) that coalesced by ~1.0 Ga into the stable core of North America (Whitmeyer and Karlstrom, 2007). Sustained tectonic tranquility continued until the Late Cretaceous, when the Laramide Orogeny triggered extensive shortening of Precambrian basement (Dickinson and Snyder, 1978). The cause of the Laramide Orogeny is thought to be shallowing of the subducting Farallon slab starting around 75 Ma (Bird, 1988). The Laramide slab trajectory, reconstructed based on plate models, seismic tomography, and geologic reconstructions (Saleeby, 2003; Bunge and Grand, 2000; Humphreys et al., 2015; Liu et al., 2010), passed beneath much of southern California, Arizona, and northward into Colorado, Wyoming, and possibly Montana.

Stark tectonic and geochemical shifts throughout the lithosphere mark the transition from pre- to post-Laramide conditions. Lower crustal and mantle xenoliths erupted during the Paleozoic at the southeastern edge of the Wyoming Craton are predominantly anhydrous (Eggler et al., 1987) and reflect stabilized lithosphere that originally accreted in the Proterozoic (Farmer et al., 2005; Chin et al., 2020a, 2020b). These xenolith systematics indicate that, until the Laramide event, much of the Wyoming Craton lower crust and upper mantle reflected stable continental lithosphere. However, post-Laramide, evidence of newly accreted oceanic lithosphere occur as exhumed Rand-Orocopia-Pelona Schist in southern California and Arizona (Jacobson et al., 1996; Chapman, 2017). Nd isotopes of peridotite xenoliths erupted in the Pliocene-Pleistocene suggest Farallon lithosphere may have been accreted beneath the Mojave Province (Luffi et al., 2009). Further to the northeast, peridotite xenoliths erupted through the Colorado Plateau in the Eocene have some of the highest water contents (Li et al., 2008) in nominally anhydrous minerals (NAMs) of any known mantle xenolith suite worldwide (Peslier et al., 2017). Passage of the Farallon slab beneath the Colorado Plateau is thought to be responsible for this mantle hydration (Hoover et al., 2020). Towards the termination of the flat slab trajectory beneath the Wyoming Craton, a number of kimberlites – some diamond-bearing – erupted in the Eocene. The Absaroka volcanism, which erupted through the central Wyoming Craton, also occurred around this time; it has been linked to melting of subduction-metasomatized mantle (Feeley, 2003). Numerical models suggest that, if flat subduction was rapid enough, the slab could retain and transport hydrous phases ~1500 km away from the trench, providing a potential deep source for volatile-rich kimberlitic magmatism (Currie and Beaumont, 2011). Disturbed Sr and Nd isotope systematics in peridotite xenoliths erupted in Eocene kimberlites in Montana indicate significant metasomatism occurred during the Mesozoic, most likely related to the Laramide Orogeny (Carlson et al., 2004).

The deep imprint of the Laramide apparently continues to geologically recent times, manifested by amphibole and mica-rich granulite xenoliths (possibly hydrated during the Laramide) erupted in ~1 to 3 Ma lamproites in the southwestern Wyoming Craton at the Leucite Hills (Farmer et al., 2005; Lange et al., 2000). In addition, an expansive survey of volcanic rocks younger than 40 Ma across the southwestern US by Farmer et al. (2020) shows distinctive Ta/Th ratios that are best explained as small-volume melts of hydrous-metasomatized lithosphere containing rutile and apatite, attesting to the persistence of subduction-modified lithosphere beneath a large swath of the western US.

## 3. Montana peridotite xenoliths

### 3.1. Overview

Peridotite xenoliths of various types occur within hypabyssal and extrusive rocks (kimberlites, lamproites, alnoites, and carbonate-rich breccias; Hausel (1998)) of the Montana alkalic province which overlies the Wyoming Craton (Fig. 3). Xenoliths from three diatreme clusters of Eocene age (O'Brien et al., 1995) – Porcupine Dome, the Grass Range

intrusions (location of the Homestead kimberlites), and the Missouri Breaks diatremes (location of the Williams, MacDougal Springs mica peridotite diatreme, and Squaw Creek) – have been previously studied for mineral major element chemistries and analyzed for final P-T by Hearn (2004) (Fig. 4).

We focus here on mantle xenoliths from the Homestead and Williams kimberlites (Fig. 3). Phlogopite K—Ar dating of the Williams diatreme yielded an age of 47.5 ± 1.6 Ma, consistent with inclusions of other local middle Eocene volcanic rocks in the kimberlite (Hearn and McGee, 1984). The Homestead kimberlite is thought to be similar in age based on a phlogopite $^{40/39}$Ar date of 51.41 Ma of the nearby Yellow Water Butte (Mitchell et al., 1991) and a K/Ar age of 50.2 Ma of the Winnett alnoitic sill (Hausel, 1998; Marvin et al., 1980). Upper mantle peridotite xenoliths are abundant at both Homestead and Williams.

Lithological classification schemes have varied between different studies of the Homestead and Williams kimberlites, but a large proportion of the peridotite types are harzburgites. Hearn (2004) noted several Homestead peridotites contain minor to trace phlogopite in various

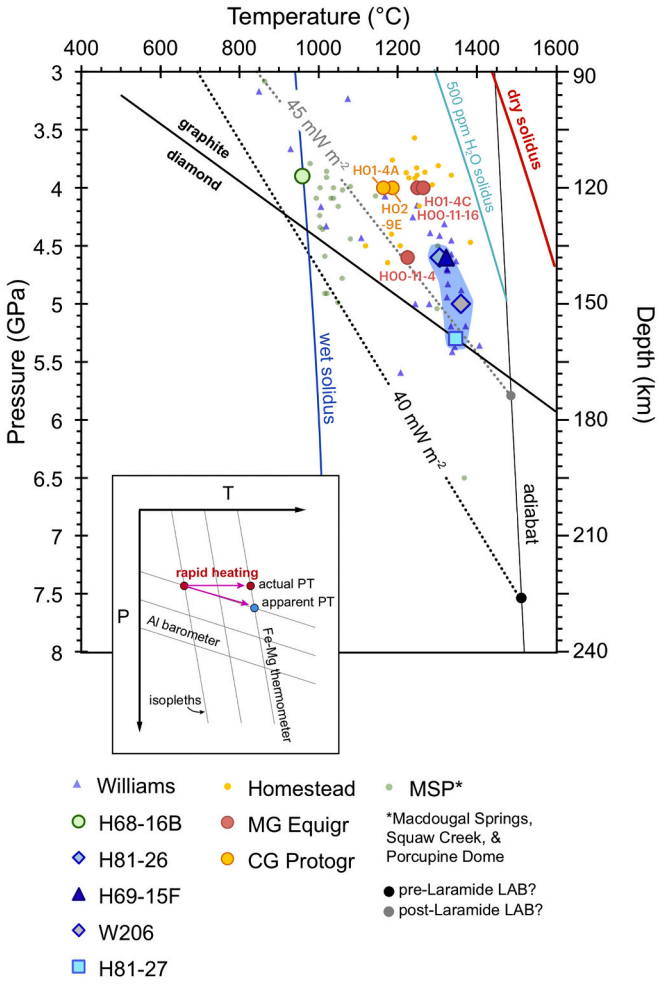


**Fig. 4.** P-T diagram of garnet-bearing peridotites from Homestead, Williams, the Missouri Breaks diatremes, and Porcupine Dome. Small symbols are xenoliths with reported final PT but no EBSD or mineral water content data; larger symbols are the samples analyzed in this study for which PT data are available. Sample names for Homestead xenoliths analyzed in this study shown. All PT data (including for samples in this study) are from Hearn (2004). Inset shows hypothetical situation of rapid heating of mantle lithosphere from a steady-state geotherm to a "false adiabat" caused by kinetic lag between Al-based barometry and Fe—Mg based thermometry. Dry and wet solidi were calculated using Hirschmann (2000) and Katz et al. (2003), respectively. MG Equig = medium-grained equigranular; CG Protogr = coarse-grained protogranular.

morphologies (dispersed grains, rims around garnet, or in clinopyroxene-spinel clots with symplectite textures suggesting decompression). Homestead xenoliths also lack porphyroclastic textures, in contrast to xenoliths from Williams which have 50% or more xenoliths identified as porphyroclastic (Hearn and McGee, 1984).

Previous xenolith work on the Homestead, Williams, and other diatremes nearby show broad groupings in P-T space (Hearn, 2004). Xenoliths from Porcupine Dome, erupted closest to the craton interior, record pressures between ~4 to ~5 GPa and temperatures ~1000 °C and fall more or less along a shield geotherm (Fig. 4). Xenoliths from Macdougal Springs (in the Missouri Breaks area, which also includes Williams) are extensively carbonated and altered; final equilibration P-T's span a wide range but all appear to fall near a shield geotherm. The Williams kimberlites contain two xenolith groups, a low-T and a high-T group (Carlson et al., 2004). The former lies along the shield geotherm, whereas the latter exhibit T's > 1200 °C, overlapping the peridotites from Homestead which all have T's between 1160 and 1390 °C (Hearn, 2004) (Fig. 4). Final equilibration pressures of Williams xenoliths are higher than those at Homestead (Fig. 4).

Our study examines 16 peridotite xenoliths from the USGS (Reston) and Smithsonian repositories (Table 1). 15 xenoliths were analyzed for mineral major, trace, and water contents, and 11 xenoliths for whole-thin section EBSD maps.

### 3.2. Lithotypes and optical petrography

#### 3.2.1. Homestead: protogranular & equigranular

In general, the Homestead xenoliths we studied are not significantly altered; extensively serpentinized xenoliths were avoided. Textures are granular, either coarse-grained protogranular (average olivine grain size 5–10 mm) or medium-grained equigranular (average olivine grain size 2–5 mm). The former represents the Primary protogranular (Pr) texture, exemplified by xenoliths H02-9E (Fig. 2a; Fig. 5a-b) and H00–12-1, H01-4A (SI Fig. 1). The latter represents the mosaic equigranular (Eq) texture of Mercier and Nicolas (1975), which would be classified within the "coarse granular" type of Boullier and Nicolas (1975). Xenoliths H00–11-16 (Fig. 5c-d) and H00–11-23 represent examples of the medium-grained equigranular texture. In H00–11-16, porphyroclasts are absent and all phases exhibit a more or less uniform grain size. Grains are amoeboid in habit, with a few 120° triple junctions. The medium-grained equigranular xenoliths studied here tend to be more serpentinized (Fig. 5c, 7), compared to the coarse-grained protogranular xenoliths (e.g. Fig. 5a); however some protogranular xenoliths are also serpentinized.

In the coarse-grained protogranular group, most of the peridotite consists of large, anhedral olivine grains (~1 cm) with interlobate grain shapes suggesting grain boundary migration recrystallization (Passchier and Trouw, 2005). Modest alignment of orthopyroxene and garnet grains define a weak lineation. The garnets have complex, cryptocrystalline kelyphitic rims probably associated with decompression in the host magma. The medium-grained equigranular xenoliths tend to have more clinopyroxene and garnet (e.g., sample H00–11-16; Fig. 5d), although lherzolites also occur in the protogranular group (Table 1). The equigranular xenoliths are characterized by medium-grained subhedral olivine with equigranular – interlobate grain boundaries grading into occasionally polygonal grain boundaries (Fig. 5c). Clinopyroxene and garnet are often spatially associated and form loosely defined bands that define a weak to moderate lineation (Fig. 5d). Orthopyroxene also forms weak bands aligned with clinopyroxene and garnet (SI Fig. 1), but orthopyroxene grains may also be dispersed throughout the peridotite.

#### 3.2.2. Williams: porphyroclastic, transitional-tablet, and tabular equigranular

We analyzed in detail 6 fresh Williams garnet harzburgites: H68—16B, H81–27, H93—11B, H81–26, W206, and H69—15F. Additional microstructural analyses on these xenoliths are also published in

**Table 1**
Summary of xenoliths analyzed in this study.

| # | Xenolith | Mineralogy | Texture | Data | NAM $H_2O$, TE | | | |
|---|---|---|---|---|---|---|---|---|
| Homestead | | | | | | | | |
| 1 | H00–12-1 | Gt-sp hzb w/ cpx, trace phl | Protogranular | EBSD | Ol | Cpx | Opx | Gt |
| 2 | H00–11-23 | Spinel hzb w/ cpx | Equigranular | EBSD | Ol | Cpx | Opx | |
| 3 | H00–11-16 | Gt-sp lhz w/ large gt | Equigranular | EBSD | Ol | Cpx | Opx | Gt |
| 4 | H01-4A | Gt lhz | Protogranular | EBSD | Ol | Cpx | Opx | Gt |
| 5 | H02-9E | Gt hzb w/ cpx | Protogranular | EBSD | Ol | | Opx | Gt |
| 6 | H01-4C | Gt lhz | Equigranular | | Ol | Cpx | Opx | Gt |
| 7 | H00–11-4 | Gt hzb w/ cpx | Equigranular | | Ol | Cpx | Opx | Gt |
| 8 | H00–11-9 | Gt-sp hzb w/ sparse cpx; opx-rich | Protogranular | | Ol | Cpx | Opx | Gt |
| 9 | H00–10-32 | Sp-phl hzb w/ cpx, coarse opx | Protogranular | | Ol | | Opx | |
| 10 | H01-4B | Gt-sp hzb w/ cpx | Protogranular | | Ol | Cpx (no TE) | Opx | Gt |
| Williams | | | | | | | | |
| 11 | H68-16B | Gt-sp-phl hzb | Tabular equigranular | EBSD | Ol | Cpx | Opx | Gt |
| 12 | H81–27 | Gt hzb | Porphyroclastic | EBSD | Ol | Cpx | Opx | Gt |
| 13 | H93-11B | Gt hzb | Porphyroclastic/Transitional-tablet | EBSD | Ol | | Opx | Gt |
| 14 | H81–26 | Gt hzb | Porphyroclastic/Transitional-tablet | EBSD | Ol | Cpx | Opx | Gt |
| 15 | H69-15F | Gt hzb | Porphyroclastic/Transitional-tablet | EBSD | Ol | Cpx | Opx | Gt |
| 16 | W206 | Gt hzb | Porphyroclastic/Transitional-tablet | EBSD | No geochemical data for this sample | | | |

Gt = garnet, sp. = spinel, cpx = clinopyroxene, phl = phlogopite; hzb = harzburgite, lhz = lherzolite; lithological classifications from Hearn (2004).
TE = trace elements.

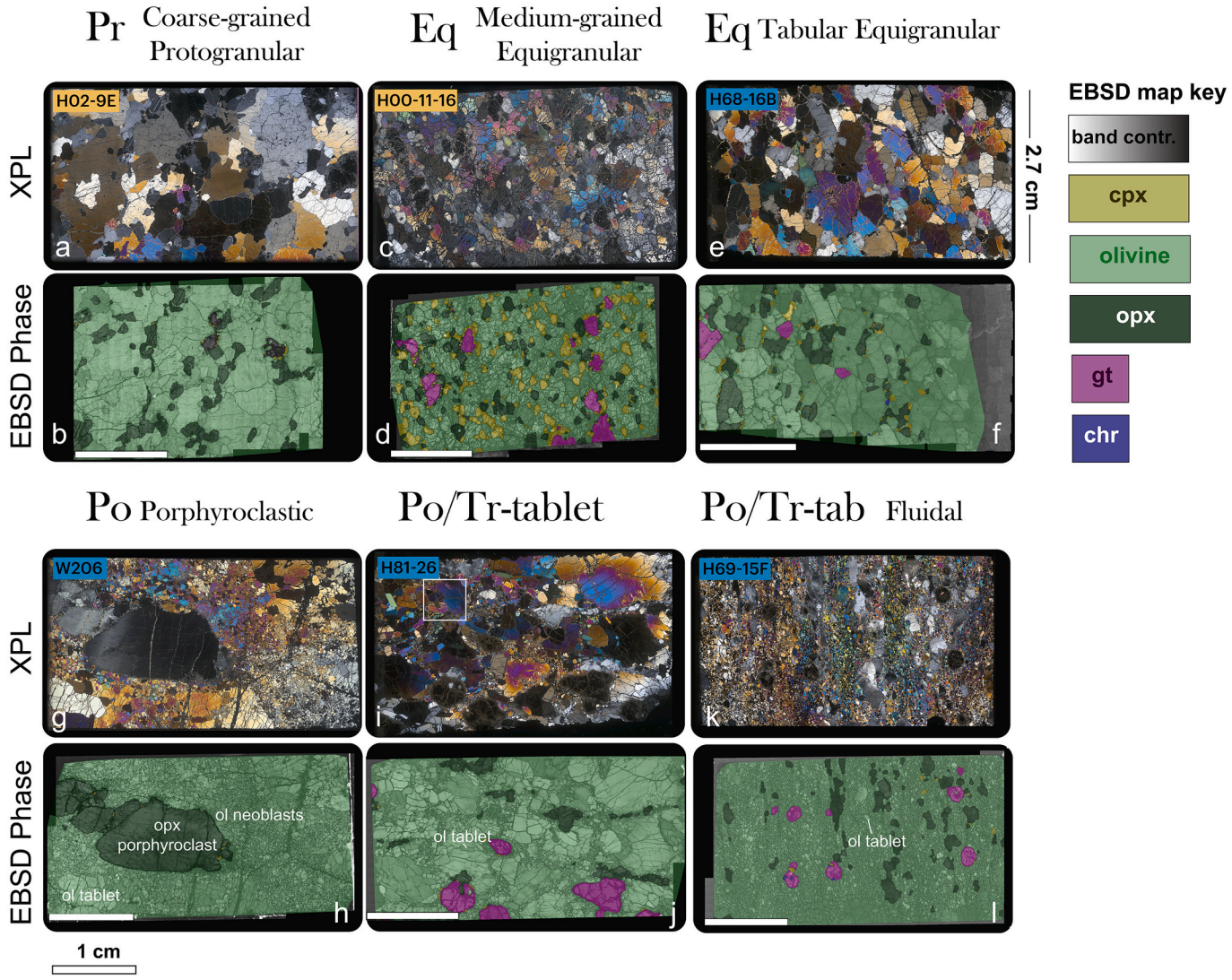


**Fig. 5.** Optical thin section scans in cross-polarized light of representative Homestead (orange text label) and Williams (blue text label) xenoliths. Below thin section scans are shown EBSD phase maps with reconstructed mineral grains (color key on bottom of figure). The mineral phase colors are superimposed on band contrast.

Boneh et al. (2021). The Williams xenoliths have textures encompassing the porphyroclastic (Pr), transitional-tablet, and tabular equigranular (Eq) textural types of Mercier and Nicolas (1975) (Fig. 1, 2).

The porphyroclastic texture is represented in xenoliths H81–27, W206 (Fig. 5g-h), and H69—15F (Fig. 5k-l). Large (>10 mm) orthopyroxene and/or clinopyroxene porphyroclasts are interspersed throughout a fine-grained (10–100 μm) recrystallized olivine matrix. In some cases, the orthopyroxene porphyroclasts are strained and bent as in W206 (Fig. 5g). One xenolith, H69—15F, shows elements of both the porphyroclastic texture originally described in Mercier and Nicolas (1975), such as intensely strained orthopyroxene porphyroclasts which appear to have "flowed" around circular garnets (Fig. 5k), and thus convey an overall fluidal mosaic texture as described in Boullier and Nicolas (1975).

Xenolith H93—11B is an excellent example of the transitional-tablet texture (Fig. 2c). An example of tablet olivine grains is shown in Fig. 6. In this microphotograph the tablet lacks evidence of intragrain strain (subgrains, undulose extinction), and the texture suggests that the grains are "growing" into a previously strained grain.

An example of the tabular equigranular texture of Mercier and Nicolas (1975), analogous to the coarse tabular texture of Boullier and Nicolas (1975), is illustrated for sample H68—16B (Fig. 5e-f). This xenolith is composed primarily of coarse-grained, tabular (~5 mm x ~ 2 mm) olivine grains containing obvious internal misorientations (Fig. 2d), and forming a shape preferred orientation that defines a macro-scale foliation.

## 4. Analytical methods

### 4.1. Sample preparation & identification of structural elements in xenoliths

A major disadvantage of microstructural analyses on xenoliths is that they often lack a clear-cut kinematic reference frame. Thus, prior to microstructural analysis, care was taken to identify as best as possible lineation and/or foliation in the xenoliths and to cut hand specimens parallel to lineation and perpendicular to foliation. When present, elongated secondary minerals, typically spinel grains and flattened pyroxene grains, were used to define an apparent lineation or foliation specific to the sample. Most hand specimens were large (~10 cm in diameter or greater), yet despite the large sizes, several xenoliths were generally too coarse-grained to unambiguously identify structural elements. In these cases, we infer the trace of the foliation plane based on crystal orientation maps (specifically, inverse pole figure or IPF maps; discussed below) that exhibit shape alignment of mineral grains (Figs. 7, 8). This was done in tandem with observations of the olivine and orthopyroxene CPOs, plotted on pole figures that have not been rotated and reflect the mineral orientations in the sample as it was mapped. We choose not to rotate pole figures to commonly used conventions (e.g., E-W representing lineation) to facilitate easy comparisons of the pole figures and large-area EBSD maps, which are shown throughout this paper in their entirety (e.g., thin section 2:1 aspect ratio).

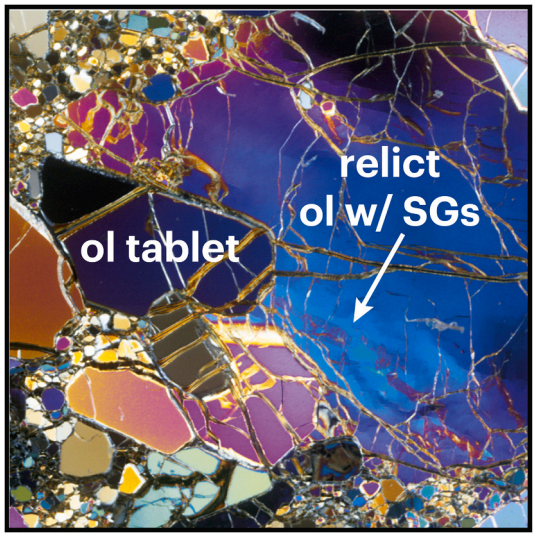


**Fig. 6.** Example of a strain-free olivine tablet impinging on a strained olivine porphyroclast from sample H93—11B (white box in Fig. 5i; refer therein for scale).

### 4.2. Electron backscatter diffraction (EBSD) mapping

Fully automated electron backscatter diffraction (EBSD) maps were collected on all xenoliths using an Oxford Instruments Symmetry EBSD detector on a FEI Apreo LoVac field emission gun scanning electron microscope (SEM) at UC San Diego. Step sizes varied from 1 to 5 μm, at working distance between 26 and 28 mm, current of 26 to 51 nA, and accelerating voltage of 20 kV. Raw EBSD data were cleaned in CHANNEL5 by first removing wild spikes, then orientations of non-indexed pixels were iteratively filled using a nearest neighbor filling method (down to 5). In most cases, cleaning was minimal or unnecessary as indexing rates were at least 90% or better. We used the open source MTEX software (versions 5.1.1 and 5.5.0) to generate and analyze the data in the EBSD maps (Hielscher and Schaeben, 2008; Bachmann et al., 2011).

### 4.3. Mineral chemistry

#### 4.3.1. Water content: secondary ion mass spectrometry

Water contents in olivine and pyroxene grains were measured using secondary ion mass spectrometry (SIMS) on a CAMECA IMS 6F at the Carnegie Institution for Science. Mineral grains were hand-picked from lightly crushed portions of each sample based on optical clarity under a stereo microscope. The grains were then embedded in indium-filled aluminum disks, which also included one standard grain to monitor instrumental drift (basaltic glass MORB, ALV 519–4-1, 1700 μg/g H2O) and one grain to determine detection limits (commercially available Suprasil 3002, pure $SiO_2$ glass, 1 μg/g $H_2O$). Mounts were polished and then cleaned with milli-Q™ water and ethanol and stored in a 50 °C vacuum oven for at least 12 h. The gold-coated samples were analyzed using a primary $Cs^+$ beam at 10 kV and 20 nA with a secondary extraction voltage of −5 kV. Although sputtering pits were ~ 30 μm in diameter, we limited ion transmission to the centermost 10 μm of the pit using the smallest available field aperture. Pre-sputtering for 300 s was used to minimize surface contamination. In addition, $^{12C/30}Si$ was measured to monitor contamination due to cracks and dust during analysis. $H_2O$ measurements of the Suprasil standard glass, which represents the blank, were 2.9 ± 3.5 (2σ) ppm. Orthopyroxene and olivine calibration curves were reported in Boneh et al. (2021). Information on all standards used and calibration curves for garnet and clinopyroxene are reported in SI Fig. 2.

#### 4.3.2. Major elements

After SIMS analyses, we measured major element oxide concentrations of the indium-mounted clinopyroxene and garnet mineral separates. We situated measurement spots as close as possible to the ion probe pits, with most spots situated as close as ~10 μm and some as far as 30–40 μm if cracks, scratches, inclusions were present. Analyses were made using the CAMECA SX100 electron microprobe (EPMA) at Brown University. In-house standards used for calibration were Natural Bridge diopside (Si and Ca); rutile, Brown University (Ti); Kakanui pyrope, NMNH 143968 (Al); synthetic $MgCr_2O_4$ (Cr); Rockport fayalite, NMNH 85276 (Fe); rhodonite, AMNH 104738 (Mn); synthetic $Fo_{97}$ forsterite, University of Rhode Island (Mg); Amelia albite, Purdue University (Na); Nickel metal, SPI 02751-AB (Ni). Secondary standards used were Lunar Crater augite, NMNH 164905, San Carlos olivine, NMNH 111312–44,

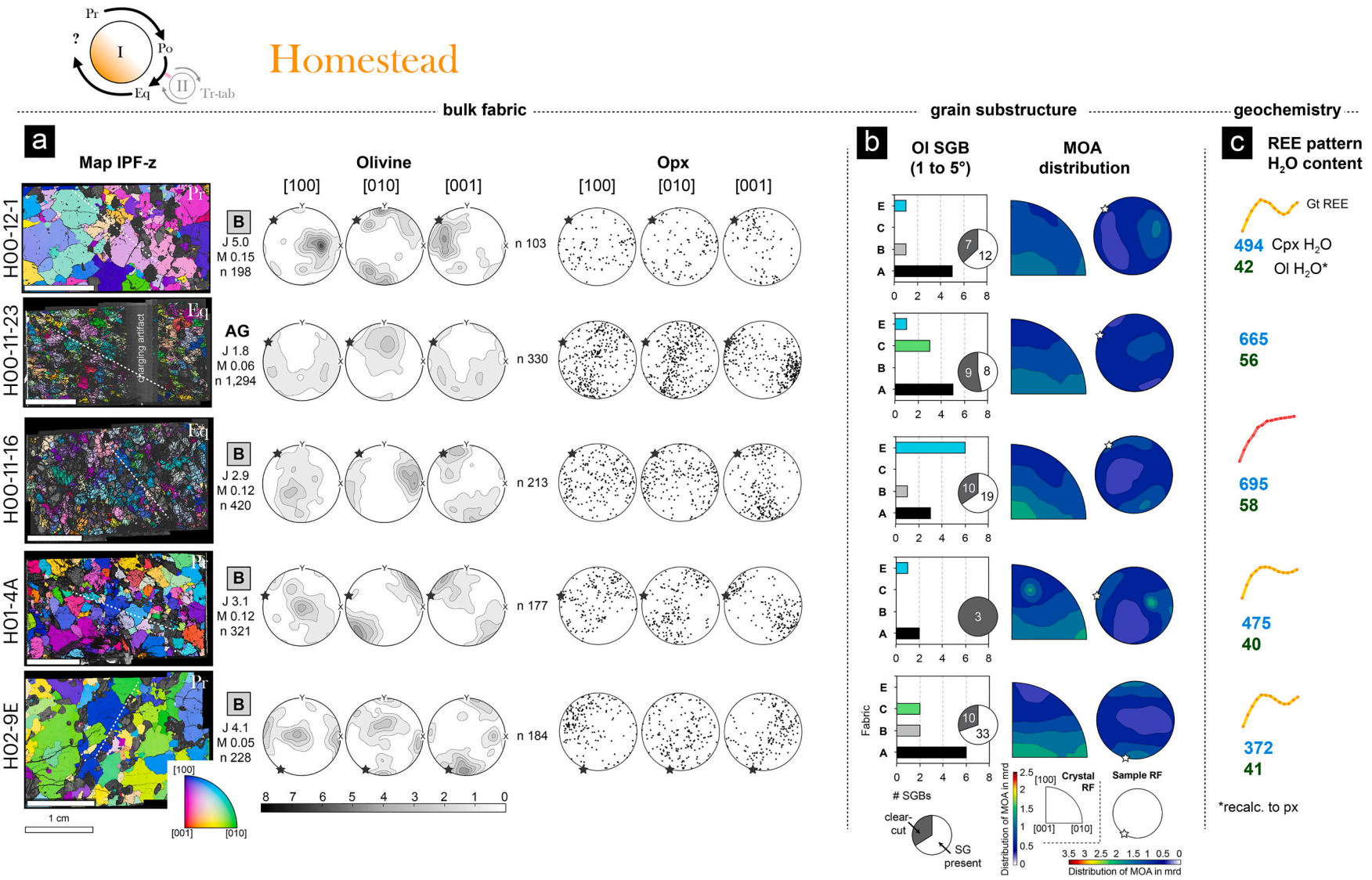


**Fig. 7.** Summary figure of EBSD data and selected mineral chemistry for Homestead xenoliths. From far left: (a) Thin section IPF-z maps showing olivine crystallographic orientations in the sample reference frame (IPF key at bottom; 1 cm scalebar applies to all maps); olivine CPOs plotted on equal-area, upper hemisphere pole figures; orientation distribution functions are plotted using a de la Vallée Poussin kernel, halfwidth 10°, contours at 1 multiple of a uniform distribution, upper hemisphere; orthopyroxene CPO (individual grains plotted). In (b), bar charts show distribution of olivine subgrain boundary (SGB) fabric types; pie charts indicate number of subgrains in each xenolith that could be unambiguously identified ("clear-cut", see text for details). In (c) is given a summary of the mineral geochemistry: garnet REE pattern (from Fig. 16) and clinopyroxene and olivine (recalculated to pyroxene) water contents. Garnet REE patterns are the same as in Fig. 16 but axes with element labels have been omitted for clarity.

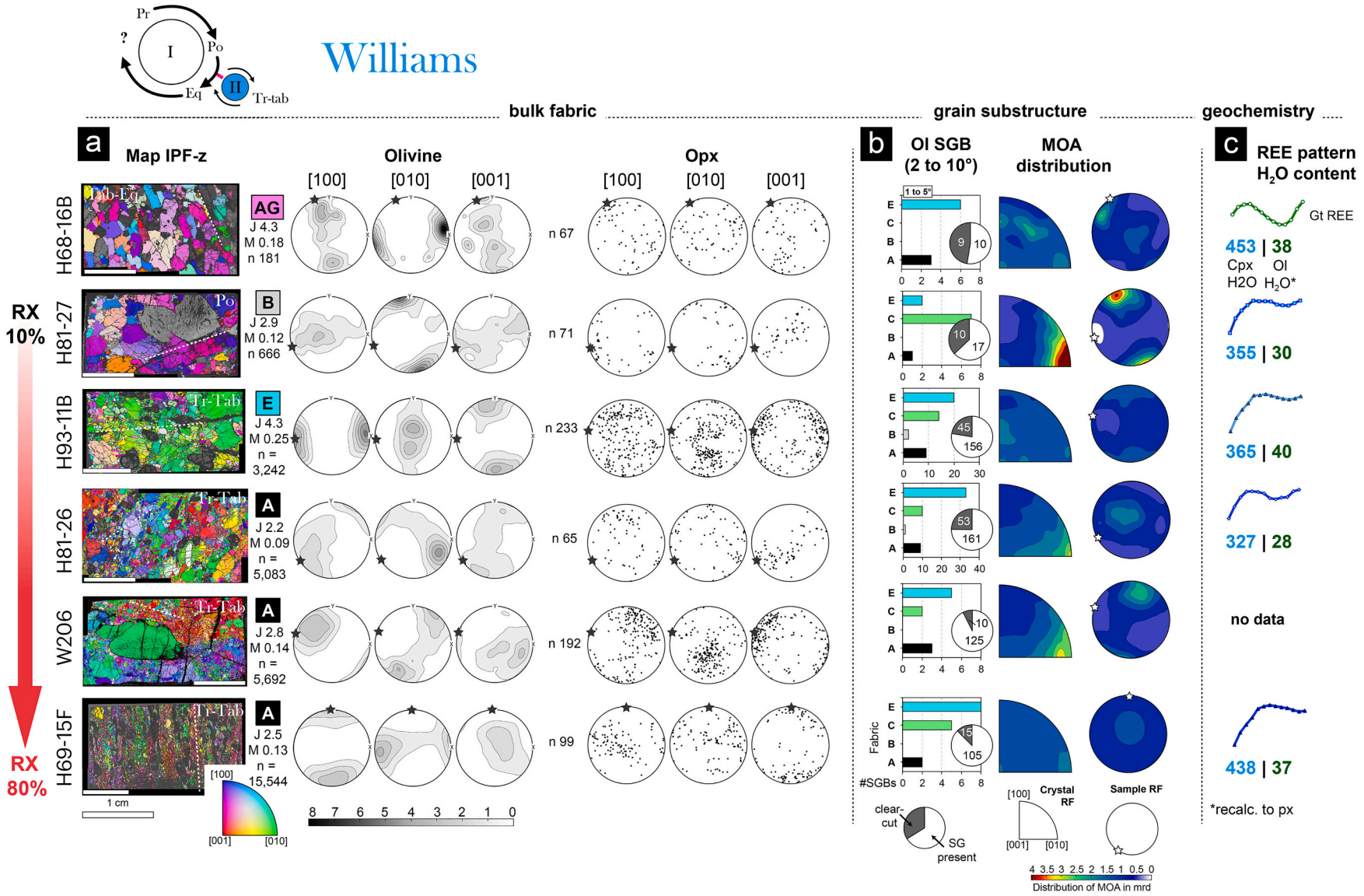


**Fig. 8.** Summary figure of EBSD data and selected mineral chemistry for Williams xenoliths. Figure structure follows that of Fig. 7. The red gradient arrow indicates amount of recrystallized grains (RX) in each sample from Boneh et al. (2021).

and Kakanui pyrope. The relative standard deviation (RSD) on precision is less than 2% for major elements, and 2–6% for minor elements, except for Mn in Kakanui pyrope (9.46%). All analyses were corrected for instrumental drift using standards with known homogeneous values.

#### 4.3.3. Trace elements

After SIMS and EPMA analyses, we employed laser ablation inductively coupled plasma mass spectrometry (LA-ICP-MS) to measure minor and trace element concentrations of indium-mounted clinopyroxene and garnet mineral separates. Laser ablation spots were measured as close as possible to the ion probe pits, with most spots located at a similar proximity to ion probe pits as the EPMA spots. Measurements were performed at Brown University using a Photon-Machines Analyte G2 Laser in conjunction with a Thermo X-series-2 quadrupole ICP-MS. Samples were ablated by a 193-nm excimer (ArF) laser with a fluence of 3.75 J/cm$^2$ and a 10 Hz repetition rate at 50% energy. Ablation duration lasted 40 s, which was preceded by 30 s of background collection. Laser spot sizes were 65 μm for garnet and clinopyroxene. All data was calibrated against glass standards from the USGS (BIR-1G, BCR-2G, BHVO-2G). We used $^{26}$Mg as an internal standard. RSD values for external precision of all standards were typically less than 10% for elements that had concentrations of at least 10 ppm, and typically less than 35% for elements with concentrations below 10 ppm.

## 5. Analysis & results: microstructures

### 5.1. Analysis strategy: large area mapping, pole figure plotting, and grain reconstruction

Large-area EBSD maps of nearly the entire thin sections were done for 11 representative xenoliths from each textural category. Analysis of these maps yields several datasets which are summarized in Figs. 7, 8, and 12 and discussed in this section. Figs. 7 and 8 (panels c) also contain a snapshot of the mineral geochemical data which are discussed in Section 6. Crystal orientation maps (inverse pole figure in the "z" sample direction) are shown side-by-side with olivine and orthopyroxene pole figures in panel a of Figs. 7 and 8. Pole figures were calculated as one point per grain (oppg) using the density of the orientation distribution function (ODF) with a half-width of 10° plotted on the upper hemisphere. The strength of the CPO was quantified using the dimensionless J-index (Bunge, 1982) and M-index (Skemer et al., 2005).

Grain boundaries are defined with a minimum misorientation angle of 10°, and distortions within grain interiors are quantified using misorientation with respect to the grain's mean orientation, (mis2mean). Grains with less than 10 pixels were removed, as these are interpreted as incorrectly detected grains. While most mapped thin sections yielded indexation rates of 90% or greater, serpentinized xenoliths (H00–11-23 and H00–11-16) had lower index rates due to the abundance of serpentine-filled cracks. Grain reconstruction for such samples is challenging, as cracks make it difficult to find nearest neighbors to fill grains with average orientations. For example, visual inspection of the crystal orientation maps of H00–11-23 and H00–11-16 (Fig. 7) indicates that similar crystal orientation (similar colors in the map) extend across serpentine cracks, suggesting that these areas were originally single grains. To calculate more realistic grains for serpentinized samples, we iterated the grain reconstruction and allowed the convex hulls of calculated grains to "grow" so that they "bypassed" the non-indexed serpentine-filled cracks. While this method results in some oddly-shaped extrapolated grains (SI Figs. 1, 3), this method does not affect the calculated CPO pole figures, because we plot them as oppg.

Finally, we also examined whether olivine pole figures and fabric strength varied as a function of whether oppg versus area-weighted treatment of all the pixels were plotted. These factors are particularly important for transitional-tablet xenoliths which have populations of varying grain morphology (e.g. porphyroclasts and tablets). There are subtle variations from the relict porphyroclastic grains and the tablet populations formed from the last event, and some degree of CPO dispersion due to episodes of static and/or dynamic recrystallization (see Fig. 6 in Boneh et al., 2021). However, the overall observed CPO did not significantly appear to be modified by the different population of grains and the CPO did not vary depending on the oppg vs. area-weighted treatment (SI Fig. 5).

### 5.2. Analysis strategy: Bulk CPO identification

For olivine, individual points in pole figures have been omitted for clarity; contours are plotted as 1 multiple of a uniform distribution (m.u.d.) and all xenoliths have been plotted using the same color scale, fixed at maximum of 8 m.u.d. For orthopyroxene individual points (grains) are plotted. On all pole figures, the black star represents the intersection of the trace of the foliation (as inferred from the neighboring IPF crystal orientation map in panel a of Figs. 7 and 8) with the primitive of the pole figure. Olivine intragrain misorientation (mis2mean) are shown in Fig. 2 for representative xenoliths from each textural type. The olivine mis2mean maps provide a measure of the intragrain defect structure. Each map is colored up to 10 degrees of internal misorientation relative to the mean orientation of the grain.

For analysis of the bulk CPO, we follow the nomenclature of Karato et al., 2008. In this scheme, the dominant olivine slip system responsible for the CPO is ascribed to a fabric "type"; i.e., [100](010) corresponds to "A" type, [001](010) to "B" type, [001] (100) to "C" type, [100](001) to "E" type, and [100]{0kl} to "D" type. Experiments also show that olivine fabric types are correlated with olivine water content and stress, with A-type being the driest at low stress, E-type at similar stress but higher water content, B type at high stress, and C type at high water content (Karato et al., 2008). In addition to these fabric types defined within the water content vs. stress parameter space, another fabric type, AG-type (also known as axial-[010]) is commonly observed in natural mantle peridotites (Bernard et al., 2019). AG-type fabric is attributed to deformation through coaxial compression (e.g. Tommasi et al., 2000; Mainprice, 2010) or at high melt fraction environment (Higgie and Tommasi, 2012, 2014; Chin et al., 2020a, 2020b).

### 5.3. Analysis strategy: Misorientation axes and intragrain microstructures

The analysis of crystallographic misorientations within a grain set containing internal misorientations and/or discrete low-angle subgrain boundaries can provide additional clues about the dominant slip system responsible for plastic deformation. We assess this in two ways – a global (bulk grains) analysis and a local (subgrain-based) analysis. For the former, we plot the misorientation axes (MOA) of all data points within a grain relative to the average orientation of the grain, for all grains in the sample. This method does not explicitly examine individual subgrain boundaries (which are assessed manually using the local method, discussed next). For the global method, we first define grains by boundaries with >10° misorientation and considering intragrain misorientations that are >1°. The grain reference orientation deviation (GROD) is used; it is defined as the misorientation $GROD_{i,j}$ between the orientation $o_{i,j}$ at a position $(i,j)$ and the reference or mean orientation $o_g$ of the grain the position $(i,j)$ belongs to. The resulting MOA are plotted in both the crystal reference frame and the sample reference frame (Fig. 7b, 8b). Fig. 9a is a "skeleton key" for predicted MOA distributions shown with respect to a reference sample kinematic frame, which here is assumed, for simplicity, to be simple shear with the horizontal representing the shear plane. In (1), the MOA plot in the shear plane and perpendicular to the slip direction. Such a configuration is consistent with simple shear and assuming the misorientation axes correspond to formation of tilt walls (cf. Hansen et al., 2014). In (2), the MOA plot parallel to the slip direction; this configuration is inconsistent with both a tilt boundary or a twist boundary composed of dislocations from the dominant slip system. In (3), the MOA plot perpendicular to the foliation plane; this configuration is consistent

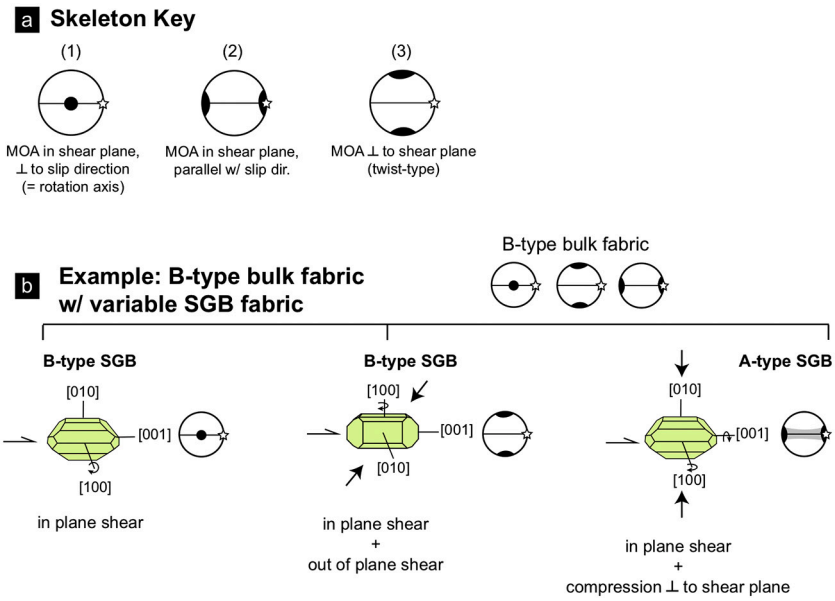


**Fig. 9.** A) Skeleton key showing hypothetical scenarios assuming simple-shear deformation and predicted misorientation axis distribution (MOA) in the sample reference frame. Shear direction is horizontal. See text for details. B) Possible scenarios in which discrepant bulk fabric and misorientation analyses may be formed. The example shown is for a peridotite with bulk B-type fabric but containing some proportion of A-type SGB. In the first scenario on the left, the kinematics are simple shear (in plane shear). The scenario in the middle is in plane shear with a component of out of plane shear, and the scenario on the right is of in plane shear with a component of compression perpendicular to the shear plane. In the case of the Williams xenoliths, the bulk CPO appears controlled by the large population of small grains with low mis2mean (Fig. 2), but the SGB are formed in the small population of large grains (porphyroclasts) with high mis2mean, which may be deforming in a different slip system different than that controlling the bulk fabric.

with the presence of twist walls, or alternatively, a more general strain geometry. We refer to Fig. 9a in the discussion of Homestead and Williams xenoliths MOA distribution in the sample reference frame.

For the local analysis of misorientations, we analyzed grains with observable subgrain (SGB) structures using the following semi-automated method. Suitable grains were found by surveying the entire population of reconstructed grains in a given xenolith, and then using individual-grain mis2mean maps (Fig. 10) to manually identify (by visual inspection) those with obvious subgrain boundaries (SI Figs. 3, 4). The trace of the subgrain boundary is then delineated on individual grain maps (Fig. 10). For Homestead xenoliths and the Williams xenolith H68—16B, grain sizes are coarse and grains contain few or subtle intragrain structures; on average we identified 8 individual grains per xenolith with subgrains for this group of xenoliths. We also restricted the misorientation range to between 1° and 5° of misorientation since intragranular microstructures are subtle in the protogranular and tabular equigranular xenoliths. For the rest of the xenoliths (all Williams except H68—16B) we identified grains containing between 2° and 10° of misorientation. Although in several xenoliths, >100 grains with subgrains are present, we restrict our analyses of misorientation across individual subgrains to examples that a) show an unequivocal crystallographic orientation for the misorientation axis (as represented by the IPF in the examples in Fig. 10) and b) dip at or near vertically in the section. The dip of the boundary was inferred by inspecting the orientation of the boundary trace in pole figures (e.g., Fig. 10), in conjunction with the observed orientation of the grain. We utilized only subgrains that appeared to dip no more than 20–25° from vertical – i.e., the pole to the plane defining the subgrain boundary trace (shown by a great circle on the pole figure) plots no more than 20–25° from the primitive. In other words, an unambiguous analysis of a subgrain boundary would show two crystallographic axes aligned with the boundary trace, one of which will have minimal dispersion (the rotation axis); the third axis (or pole to plane parallel to the boundary trace) would plot close to (<25°) or on the primitive and perpendicular to the boundary trace (Fig. 10; Precigout and Hirth, 2014; Chin et al., 2016).

An alternative method to investigate intragranular misorientations involves analysis of discrete low angle (i.e., 2 to 10°) boundary misorientations. The misorientation distribution of subgrain boundaries can be calculated using the "innerBoundary" function in MTEX. In Fig. 11, we show a side-by-side comparison of the same grain containing subgrains using the semi-automated method (Fig. 11a) versus the innerBoundary method (Fig. 11b). The latter method results in fewer discrete subgrain boundaries (170 segments) compared to interpretation by visual inspection. Additionally, the innerBoundary method cannot distinguish between intragranular cracks (i.e. due to decompression during xenolith eruption or serpentinization) and true subgrain boundaries. This is avoided in the semi-automated method which relies on the combination of user interpretation of subgrain boundaries and plotting of all pixels (i.e. all misorientations) present in the grain. The rotation axis around which the interpreted subgrain boundary forms is then confirmed using a combination of pole figures (sample reference frame) that plot the misorientation distribution and the inverse pole figure (crystal reference frame). In the case of Fig. 11a, the clear maximum at [001] in the IPF and the tight clustering of [001] axes in the pole figure make an unambiguous case for [001] as the rotation axis, indicating that the boundary is composed of edge dislocations from the [100](010) slip system. Owing to the abundance of intragranular cracks in our samples, we opted to identify subgrains using the semi-automated method.

### 5.4. *Results: Bulk olivine fabric of Homestead and Williams xenoliths*

The Homestead xenoliths show generally orthorhombic olivine CPOs with variable strength (J index ranges from 1.8 to 5.0, and M-index from 0.05 to 0.15) (Fig. 7a). The three coarse-grained protogranular xenoliths H00–12-1, H01-4A, and H02-9E show alignment of olivine [001] subparallel to both the trace of foliation and orthopyroxene [001], with olivine [010] perpendicular to the inferred foliation plane. These characteristics are consistent with B-type olivine fabric, corresponding to dominant slip on [001](010). In general, orthopyroxene deforms predominately on [001] (100) (Christensen and Lundquist, 1982), though some samples show evidence for slip dominantly on [001](010) (Baptiste et al., 2012). Thus, alignment of orthopyroxene [001] with olivine [001] supports the interpretation of olivine slip system. The equigranular xenolith H00–11-16 also shows B type olivine fabric, but the other equigranular xenolith H00–11-23 has a much weaker CPO (J-index of 1.8) characterized by weak girdles of [100] and [001] indicating an AG-type fabric.

For Williams xenoliths, the high-T Williams xenoliths (all samples except H68—16B) have orthorhombic olivine CPO with a J-index ranging from 2.5 to 4.3 and M-index from 0.09 to 0.25 (Fig. 8a). H81–26, W206, and H69—15F show olivine [100] maxima parallel to both the trace of the foliation and to orthopyroxene [001] maxima.

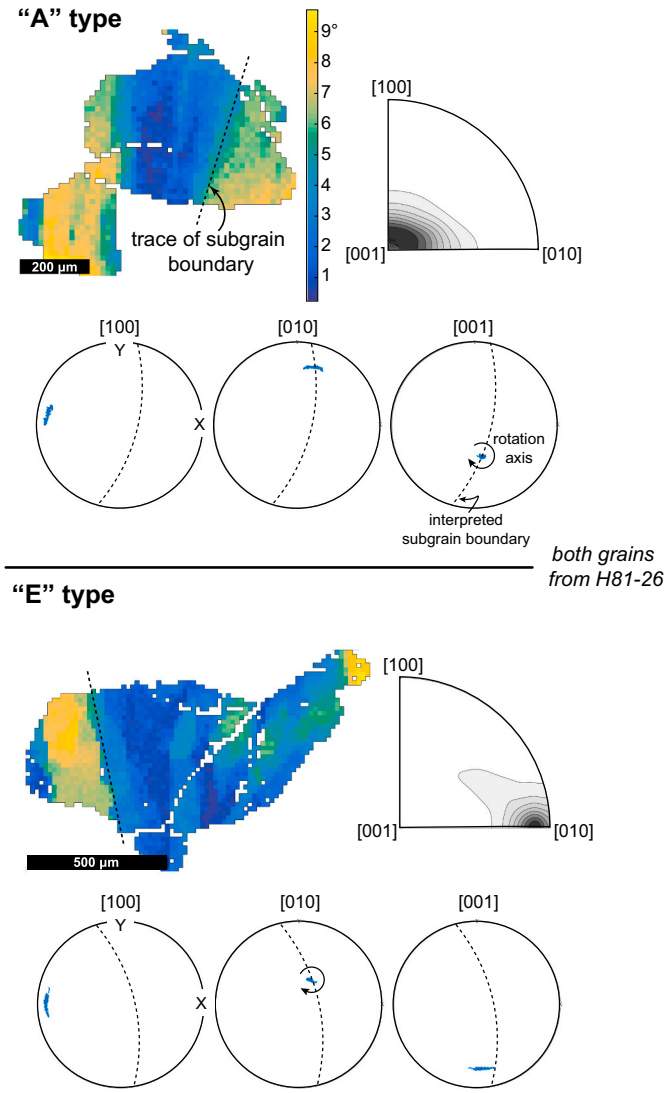


**Fig. 10.** Examples of olivine grains with clearly identifiable subgrains from Williams xenolith H81–26. Note, a total of 53 individual grains with subgrains have been characterized in this sample; we show here two representative examples for illustration purposes.

Olivine [010] maxima are approximately perpendicular to the foliation trace. These CPOs are characteristic of A-type fabric, corresponding to dominance of the [100](010) slip system. H93—11B shows an olivine [100] maximum parallel to trace of foliation and to the orthopyroxene [001] maximum, but with olivine [001] maximum perpendicular to the foliation trace, indicating E-type fabric. H81–27 has an olivine [001] maximum parallel to foliation trace and the orthopyroxene [001] maximum, and the olivine [010] maximum perpendicular to foliation trace; these features indicate a B type fabric. Finally, H68—16B is characterized by a girdled distribution of olivine [100] and [001] with a strong [010] maxima perpendicular to foliation trace. Orthopyroxene grains show a weak alignment of [100] axes parallel with the foliation trace. We characterize the CPO of H68—16B as an AG-type.

### *5.5. Results: Misorientation axes (MOA) and intragrain microstructures of Homestead and Williams xenoliths*

The statistics for subgrain microstructures (e.g., local misorientation analysis) are summarized in bar plots and inset pie charts in Fig. 7b and Fig. 8b for Homestead and Williams, respectively. These individual bar plots are also summarized for the entire Wyoming suite in Fig. 12, where we show both the distribution of subgrain fabric types and their correspondence to bulk fabric type. Within the same figure panels of Fig. 7b and 8b, we also plot the distribution of global MOA in the crystal reference frame (plotted as IPFs) and sample reference frame (plotted as pole figures).

In Homestead protogranular xenoliths, global MOA IPFs show a distribution between [001] and [010], consistent with tilt walls for A-type ([001] rotation axis), and C-type ([010] rotation axis), and twist walls for B-type ([010] rotations) (cf. Chin et al., 2016). The maxima in the IPFs are also generally consistent with the analyses of discrete subgrain structures (Fig. 7b) that show a large number of A-type subgrains, but also other types. Using the "skeleton key" of Fig. 9a, we find that all three cases are represented in Homestead. The only xenolith showing case (1) is H00–11-23 (AG-type fabric). Case (2) is represented by 3 xenoliths: H00–11-16 (B-type fabric), H01-4A (B-type fabric), and H02-9E (B-type fabric). Case (3) is represented by H00–12-1 (B-type fabric).

For Williams, global MOA IPFs show a distribution generally clustered at or near [010] (Fig. 8b). This is consistent with the predominance of C- and E-type discrete subgrains which necessitate a [010] rotation axis (Fig. 8b), but is at odds with the observed A-type bulk olivine fabric which should predict dominantly [001] misorientation axes. We

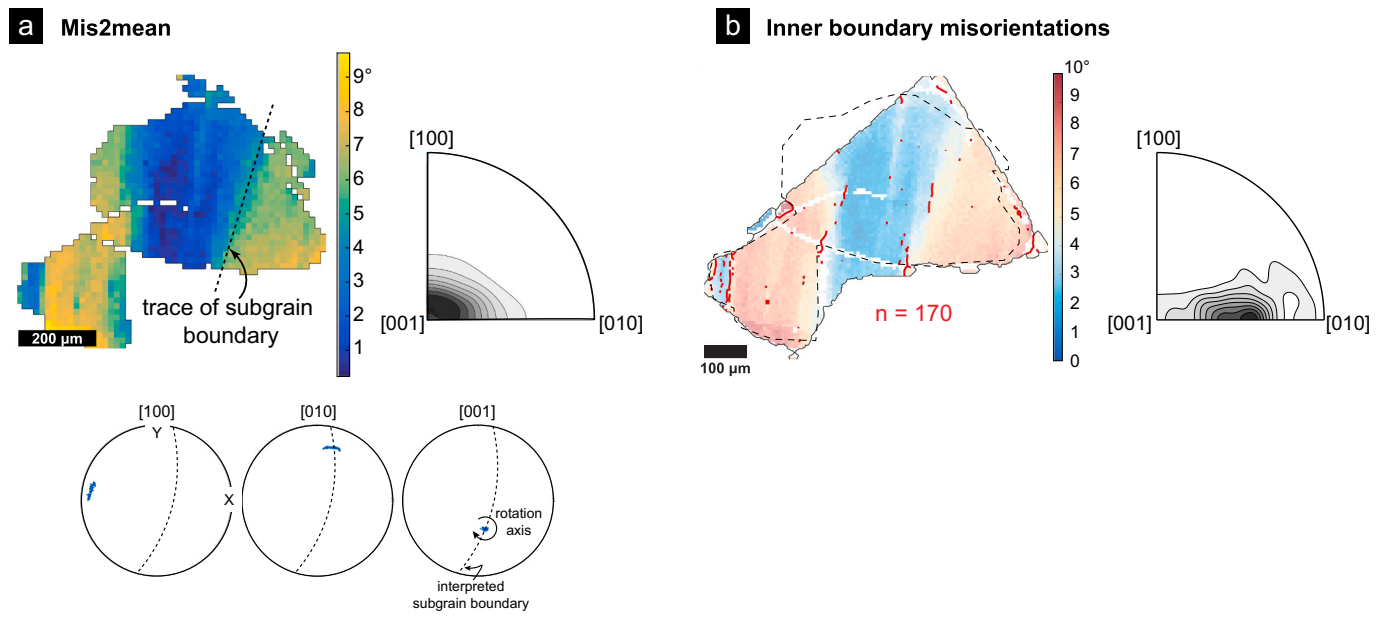


**Fig. 11.** Intragranular misorientation analyses of grain with "A" type fabric from Fig. 10. A) semi-automated method using mis2mean grain maps and associated pole figure and inverse pole figure (IPF) plotting all low-angle misorientations. B) "innerBoundary" method using discrete subgrain boundary segments. Dashed outline region approximates the reconstructed grain area from A). Note in some areas of the grain, intragrain cracks have been mistakenly identified as a subgrain boundary. IPF in both A) and B) are contoured to same intervals.

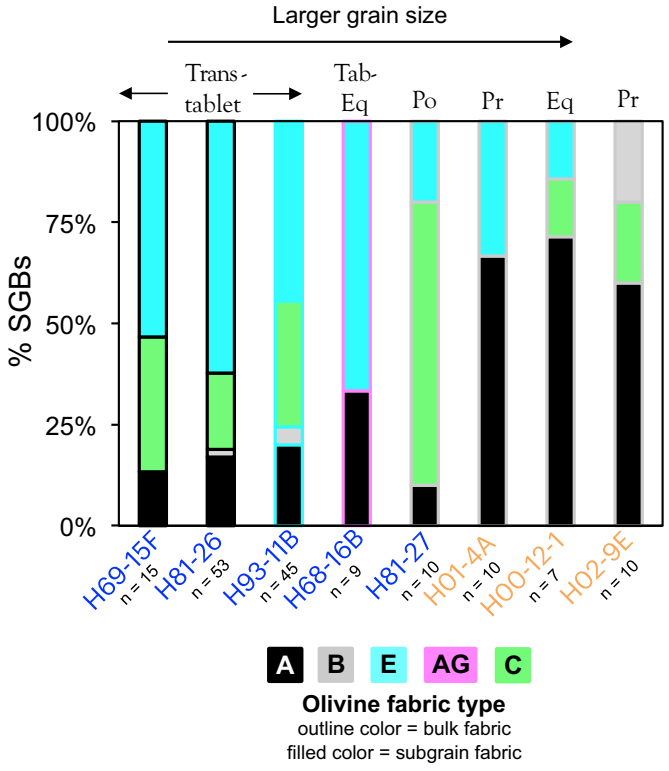


**Fig. 12.** Percentage of olivine subgrain boundary (SGB) types in Williams and Homestead xenoliths (n = number of analyzed subgrains). The outer color of the bars represents the bulk olivine fabric as determined from the olivine CPO (Fig. 7a, 8a), and the inner color of the bars represents the fabric type of the SGB. (This is the same data shown as individual bar charts in Figs. 7 and 8) but with the added information of bulk CPO superimposed.

highlight some details of Williams xenoliths here: H68—16B shows a girdle distribution in its IPF of MOA; subgrains are primarily E-type (Fig. 8b, 12). H81–27 shows a strong maximum in the IPF around [010], which is inconsistent with the observed B-type fabric (which should show a dominant [100] rotation axis). Subgrains are predominantly C-type, although a small percentage are A-type (Fig. 12). H93—11B, which has an E-type fabric, does not show a noticeable maximum around any crystallographic axis in its IPF. Subgrains are a mix of A, B, C, and E type, but the majority are E and C-type. In terms of interpreting global MOA in the sample reference frame using Fig. 9a, we also find that each of the three cases is present in Williams. Xenoliths showing case (1) are H81–26 and H69—15F (both have A-type fabric). Case (2) is represented by H68—16B (AG-type fabric). Case (3) is shown by H81–27 (B-type fabric), H93—11B (E-type fabric), and W206 (A-type fabric).

### 5.6. *Summary of CPO, SGB, MOA across Wyoming Craton xenoliths*

The analysis of bulk fabric, misorientations, and subgrain structure reveal a complex picture in the Homestead and Williams xenoliths. We have used predictions for dislocation creep in simple shear deformation as a "baseline" to frame our observations. However, few xenoliths fall neatly within this framework. For example, although the Homestead xenoliths primarily show B-type CPO, the analysis of MOA show evidence for A-type subgrains (Fig. 12), and the orientation of the MOA in the sample reference frame are mostly inconsistent with a simple shear kinematics. At Williams, the opposite picture emerges, with dominantly A-type bulk CPO and many MOA consistent with E-, or C-type subgrains. The dominant motif appears to be discrepancy between the bulk fabric and the intragranular microstructures. In the discussion, we will return to these seemingly conflicting observations and propose interpretations for them in light of geochemical and tectonic factors.

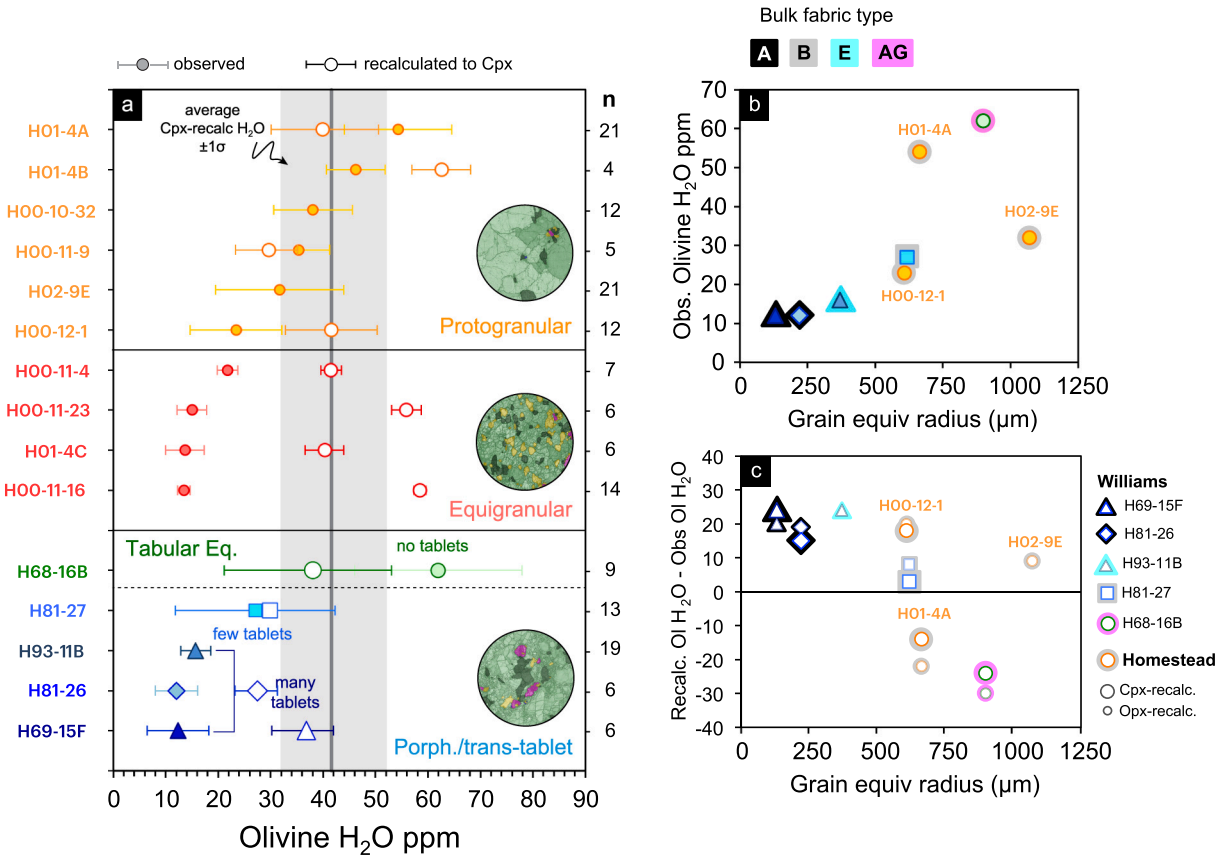


**Fig. 13.** A) Olivine water content ($H_2O$ ppm) in Homestead and Williams xenoliths. Filled symbols represent measured water content and open symbols represent recalculated water content using the Dcpx/ol = 12 (Hauri et al., 2006). N represents the number of spots analyzed in total for each xenolith (a minimum of 4 grains were analyzed for each xenolith, with multiple spots per grain). Textural classifications (protogranular, equigranular, porphyroclastic/transitional) shown for reference. B) Measured olivine water content versus average grain size (calculated using equivalent grain radius). Outer symbol color refers to bulk fabric type. C) Recalculated olivine $H_2O$ – observed olivine $H_2O$ ($\Delta H_2O$) versus average grain equivalent radius. Smaller symbols = water contents corrected to be in equilibrium with Opx; larger symbols = water contents corrected to be in equilibrium with Cpx.

## 6. Results: mineral trace element and water content

### 6.1. *Water contents in olivine, pyroxenes, and garnet*

Olivine water contents (ppm $H_2O$ by weight) for Homestead and Williams xenoliths are shown in Fig. 13 and reported in SI Table 1. Olivine water contents range from 12 ppm to 62 ppm. At least 4 individual grains with a minimum of 4 spots in areas corresponding to cores to rims of the grain were analyzed in each xenolith. This approach of spot analyses cannot resolve detailed core-rim zoning in water content.

Clinopyroxene water contents are reported in SI Table 2 and range from 327 to 695 ppm. Most xenoliths had at least 2 grains with at least 2 spot measurements, but two xenoliths, H01—4B and H00–11-23, have only 1 reported grain with 1 core measurement (SI Table 2). Orthopyroxene $H_2O$ varies from 253 to 424 ppm; data are reported in SI Table 3. As with clinopyroxene, in most cases at least 2 grains with at least 2 spot measurements were analyzed, but one xenolith (H93—11B) has 1 grain with 2 core measurements. Clinopyroxene versus orthopyroxene water contents are plotted in Fig. 14 and SI Table 4.

Garnet water contents are reported in SI Table 5 and range from 3.8 to 27 ppm $H_2O$. Two xenoliths (H00–119 and H01—4C) have only 1 measured grain with 1 core analysis. Garnet water content is plotted against clinopyroxene water content in Fig. 15.

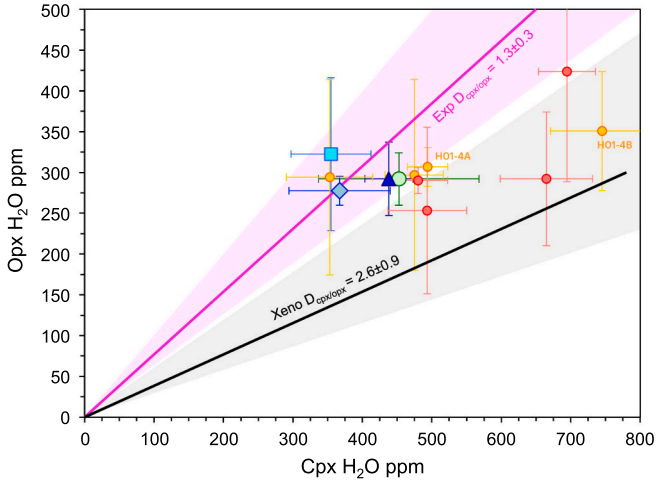


**Fig. 14.** Orthopyroxene vs. clinopyroxene water contents. Experimental Dcpx/opx and literature xenolith Dcpx/opx ranges are shown (see text for references). Symbols for Williams samples given in Fig. 13.

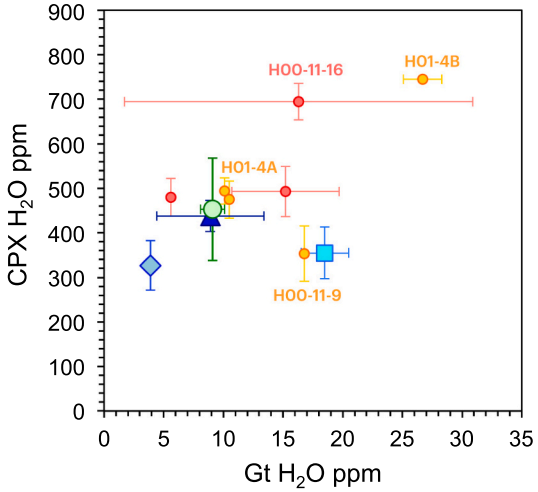


**Fig. 15.** Garnet $H_2O$ vs. clinopyroxene $H_2O$. Symbols for Williams samples given in Fig. 13.

### 6.2. Mineral major element chemistry

Hearn and Boyd (1975), Hearn and McGee (1984), and Hearn (2004) discuss in detail major element mineral compositions of garnet peridotites from the Williams and Homestead kimberlites. Our major element compositions (Supplementary Information) are similar to those previously reported by these studies. In brief, mineral compositions are broadly similar to garnet peridotites characteristic of depleted cratonic lithosphere. Olivine (SI Table 6) and orthopyroxene Mg#'s are restricted from 91 to 93. Clinopyroxene Mg#s range from 89 to 95. Garnet $Cr_2O_3$ ranges from ~2 to ~9 wt%. No major element zoning was observed in pyroxenes, garnet, or olivine in the xenoliths.

### 6.3. Mineral trace element chemistry

Primitive-mantle normalized rare earth element (REE) patterns in garnet and clinopyroxene are shown in Fig. 16a-d. All data plotted are averages per individual xenoliths and are reported in SI Tables 2 and 4. For garnet, two groups of REE patterns emerge: a "normal" pattern characterized by a monotonic increasing slope that plateaus between MREE (middle rare earth elements) and HREE (heavy rare earth elements) and a "sinusoidal" pattern characterized by a dip between MREE and HREE. Both normal and sinusoidal garnet patterns are present at Homestead and Williams. Clinopyroxene REE patterns are generally monotonic, but there is some correlation with garnet patterns. For example, H68—16B has strongly sinusoidal garnet REE and has highly LREE (light rare earth elements)-enriched clinopyroxene (Fig. 16a); H81–26 has a moderately sinusoidal garnet REE pattern and a mildly sinusoidal clinopyroxene REE pattern (Fig. 16a). Normalized clinopyroxene concentrations also generally decrease from LREE to HREE, as would be expected for equilibration with garnet.

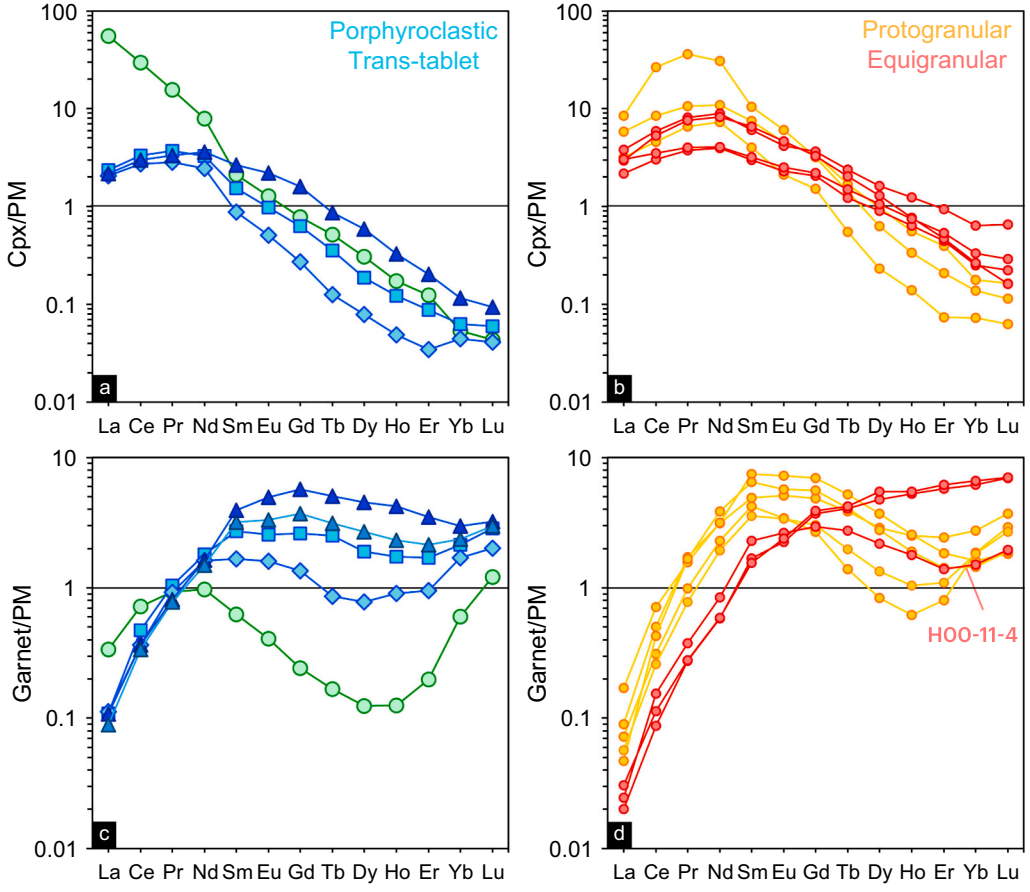


**Fig. 16.** (A-D) Rare earth element (REE) primitive-mantle normalized diagrams of garnet and clinopyroxene. Normalizing values from McDonough and Sun (1995). Symbols for Williams samples given in Fig. 13.

## 7. Analysis of mineral water content and assessment of equilibrium

### 7.1. Olivine

From the 11 EBSD mapped xenoliths, we calculated average olivine grain sizes for 8 samples and compared this to average olivine water content. The following xenoliths were excluded from the grain size vs. water content calculations: W206 (no mineral chemistry was analyzed for this sample), H00–11-23 and H00–11-16 (serpentinization prevented accurate grain size calculation).

A major concern for interpreting water contents in nominally anhydrous minerals in xenoliths is the extent to which pre-eruption mantle water contents were modified by diffusive exchange during magmatic processes. Examples of such processes include several stages of metasomatism with variable melt water content interacting with the lithospheric mantle, degassing of the melt hosting the xenoliths while en route to the surface, and diffusive loss during magmatic host emplacement. Diffusive $H_2O$ loss in olivine is usually manifested by bell-shaped diffusion profiles (e.g., Demouchy et al., 2006). Our data collection approach, which focused on measuring a large number of grains in each xenolith during an individual SIMS session, did not make it possible to resolve core-rim water zoning profiles. While spot measurements were taken within cores and at grain rims, we did not observe systematic variations across cores to rims, and in general, core and rim water contents overlap within our dataset.

At cool conditions along a cratonic geotherm (e.g., near ~1000 °C at ~150 km depth, Fig. 4), H ("water") diffusivities are similar for olivine (Demouchy and Mackwell, 2006), orthopyroxene (Stalder and Skogby, 2003), and clinopyroxene (Ferriss et al., 2016). However, Xu et al. (2019) highlight that H diffusivity in olivine increases much faster than H diffusivity for pyroxenes with increasing temperature. At ~1200 °C, H diffusion in clinopyroxene is ~2 orders of magnitude slower than for olivine; orthopyroxene lies in between the two. Therefore, at the high equilibration temperatures of the Wyoming xenoliths (>1100 °C; Fig. 4), these differences in H diffusion are significant – at such high temperatures, equilibration times of H in all NAMs are so rapid that H will equilibrate in hours over the grain scale.

Therefore, to account for the possibility of olivine water loss at the high final temperatures recorded by the Wyoming xenoliths, we recalculate the measured olivine water contents to values in equilibrium with pyroxene. Based on the analysis of Xu et al. (2019), clinopyroxene may be the most "robust" NAM to see through the "veil" of rapid diffusive water loss for high-T xenoliths. We recalculated measured olivine water contents to equilibrium values with clinopyroxene (Fig. 13a) using the partition coefficient of $D_{cpx/ol} = 12$ from the experiments of Hauri et al. (2006). (For comparison, we have also recalculated olivine water contents to be in equilibrium with orthopyroxene using $D_{ol/opx} = 0.11$ (Warren and Hauri, 2014); we show both recalculated water contents in Fig. 13c.) Most xenoliths have cpx-recalculated olivine water contents higher than the measured water contents, but 3 xenoliths (H01-4A, H00–11-9, and H68—16B) have recalculated values lower than measured (Fig. 13a). The equigranular xenoliths have, on average, the largest $\Delta H_2O$ (Recalculated – observed) out of all the xenoliths, with some samples approaching 50 ppm $H_2O$ difference. The average cpx-recalculated olivine water content is 33 ± 5.2 ppm for Williams, and 45 ± 12 ppm for Homestead.

We also explore correlations between the systematics of olivine water content and grain size. We calculated the average equivalent grain radius (the radius of a circle with the same area as the grain polygon) for the reconstructed grain populations (at least 150 grains per xenolith, Figs. 7, 8) of the Williams and protogranular Homestead xenoliths. We filtered out grains with an area less than 100 $\mu m^2$ from the calculated grain size set. The rationale behind this is that both protogranular and porphyroclastic textures are intrinsically characterized by a strongly bimodal grain size population which is further biased by the small area of standardized thin sections. In protogranular xenoliths, there is a large number of small grains that are either relict from a previously more fine-grained texture, or are forming by bulging nucleation. In porphyroclastic xenoliths, the fine-grained matrix grains are far more numerous than coarse-grained porphyroclasts. Thus, the large number of very small grains would skew the grain size average; yet these small grains make up a small fraction by total area of the sample. Our estimate of average grain size is therefore intended to capture the broadest characterization of the sample as possible. Visual inspection of thin section photos and EBSD maps (Fig. 5) were compared to calculated grain sizes. We calculated olivine grain sizes for 8 xenoliths based on EBSD maps. We did not calculate equivalent grain radii for the equigranular Homestead xenoliths, owing to the serpentinization bisecting original grains which makes accurate grain area estimates challenging (SI Fig. 3). However, inspection of the IPF maps (Fig. 7) suggests that most original grains (as represented by the same IPF color corresponding to one crystallographic orientation per grain) would plot at intermediate grain sizes between the fine-grained Williams and the coarse-grained protogranular Homestead. The measured olivine water contents are plotted versus average grain equivalent radius in Fig. 13b. An overall positive correlation is observed, suggesting a kinetic effect (i.e. larger grain sizes may have experienced less water loss).

The difference between the cpx-recalculated olivine water values and the observed values ($\Delta H_2O$) is plotted as a function of grain size in Fig. 13c. Fig. 13c shows that most xenoliths have a positive $\Delta H_2O$, suggesting diffusive loss in olivine. Two xenoliths have negative $\Delta H_2O$ (Fig. 13c), which could indicate re-addition of water to olivine. The origins of such water re-addition, if it occurred, are unclear and not resolvable with our current dataset. In summary, based on the large differences in H diffusivity between clinopyroxene and olivine at temperatures >1200 °C (Xu et al., 2019), but similar diffusivities at temperatures <900 °C, we conclude that the cpx-recalculated olivine water contents are more indicative of primary (i.e., mantle) olivine water contents.

### 7.2. Garnet

Measured garnet water contents (3.8 to 27 ppm; Fig. 15, SI Table 4) are generally lower than measured olivine water contents. Hauri et al. (2006) report a Dgt/ol value of 2.3 based on high-temperature experiments. Garnet, therefore, does not appear to be in equilibrium with olivine in the xenoliths. Garnet is also not in equilibrium with clinopyroxene, given Dcpx/gt ~ 5 (Hauri et al., 2006), whereas the ratio of clinopyroxene to garnet water contents is much higher in our dataset. Pyrope-rich garnets (similar to those in the Wyoming xenoliths) have very fast H diffusivities, similar to or faster than olivine at temperatures ~1200 °C (Reynes et al., 2018). Thus, the low measured water contents of garnet may also indicate diffusive water loss.

### 7.3. Pyroxene

While pyroxenes are generally thought to be more robust recorders of primary (i.e. mantle) water content (e.g., Warren and Hauri, 2014), there is evidence that orthopyroxene may suffer from diffusive loss to a greater extent than clinopyroxene (Tian et al., 2017). We do observe large variability in measured orthopyroxene water contents (Fig. 14), but less variability in clinopyroxene water content. This, combined with the difference in activation energy for H diffusion (Xu et al., 2019) as mentioned above, and our sampling strategy of analyzing several spots on a large number of grains, suggests that there may be significant zoning in our measured orthopyroxenes.

The inter-mineral ratio (Rcpx/opx) is defined as the ratio of measured $H_2O$ in clinopyroxene to measured $H_2O$ in orthopyroxene.

Rcpx/opx may be compared to experimental mineral/mineral partition coefficients, Dcpx/opx, calculated using experimental mineral/melt partition coefficients. This comparison can yield insights into the degree of equilibrium between clinopyroxene and orthopyroxene. We use values from Warren and Hauri (2014) – they report an averaged experimental D of 1.3 ± 0.3 (based on experiments of Aubaud et al., 2004; Tenner et al., 2009; Hauri et al., 2006; and O'Leary et al., 2010) and average literature xenolith Rcpx/opx of 2.6 ± 0.9. The ranges of experimental D, literature xenolith Rcpx/opx and our observed R values are plotted in Fig. 14. The xenoliths, particularly the Williams and the protogranular Homestead, plot within the range of experimental D's. Williams Rcpx/opx are 1.5, 1.1, 1.2, and 1.5 for H68—16B, H81–27, H81–26, and H69—15F, respectively. Protogranular Homestead Rcpx/opx are H00–12-1–1.6, H01-4A – 1.6, H00–11-9–1.2, and H01—4B – 2.1. By contrast, the equigranular Homestead xenoliths trend towards higher Rcpx/opx values, overlapping the xenolith literature field.

### 7.4. Assessment of equilibrium

Based on the analysis of water systematics in olivine, garnet, and pyroxenes, it appears that only clinopyroxene and orthopyroxene water contents reflect equilibrium at the final equilibration temperatures of the xenoliths, given the overlap of the ratio of measured water contents (Rcpx/opx) with experimental D values in Fig. 14. The low observed water content in olivine as a function of grain size (Fig. 13) and garnet (Fig. 15) suggests that both of these minerals suffered diffusive water loss. Determining the process(es) that produced diffusive loss of water in olivine and garnet cannot be resolved at this time with our current dataset; we are at present actively investigating the answer to this question. However, based on the analysis of Xu et al. (2019) and the lower scatter of $H_2O$ content in clinopyroxene compared to orthopyroxene (Fig. 14), we conclude that cpx-recalculated olivine water contents are more resilient to late-stage diffusive water loss and can be used to estimate primary mantle conditions.

## 8. Discussion

### 8.1. Laramide metasomatism and hydration

The mantle beneath Homestead and Williams xenolith experienced a complex history of metasomatism and hydration. Carlson et al. (2004) reported disturbed Sr—Nd isochrons of peridotite xenoliths at both localities consistent with metasomatic overprinting, most likely during the Mesozoic Laramide Orogeny. Our new trace element and water data also support this. First, garnet REE patterns in PM normalized diagrams show two types – a "normal" type with a monotonic pattern increasing from LREE to MREE, and a generally flat pattern from MREE to HREE; and a "sinusoidal" pattern with a dip between MREE and HREE. Both REE patterns are emblematic of silicate melt metasomatism affecting an initial melt-depleted peridotite. A metasomatic origin of garnet and clinopyroxene is supported by the positive trend in garnet versus clinopyroxene water content in Fig. 15. One interpretation of the normal versus sinusoidal garnet REE patterns is that the former reflect higher melt/rock ratios (and thus larger extent of REE equilibration between peridotite minerals and melt) and the latter lower melt/rock ratios (and thus lower extent of REE equilibration between mineral and melt).

Second, both Homestead and Williams pyroxenes have elevated water contents at low pyroxene Al(IV) contents typical of other cratonic regions, suggesting the Wyoming xenoliths experienced hydrous metasomatism (Fig. 17). The Wyoming xenoliths have orthopyroxene as hydrous or even more hydrous than Colorado Plateau xenoliths, which are thought to have suffered hydrous metasomatism by the Farallon slab during the Laramide Orogeny (Li et al., 2008). Clinopyroxene water contents of the Wyoming xenoliths also approach and overlap those of the Colorado Plateau.

Third, orthopyroxene/clinopyroxene water ratios fall within the high-temperature mineral/melt D $H_2O$ range compared to the xenolith literature range (Fig. 14). This, combined with the generally high (>1200 °C) temperatures of the xenoliths, suggests they may have last equilibrated with a silicate melt at near-solidus conditions (Fig. 4).

### 8.2. Water content of calculated melts

Using Dmineral/melt values from Hauri et al. (2006), water contents of metasomatic melt last in equilibrium with orthopyroxene are ~1.7 wt %, and water contents of melts last in equilibrium with clinopyroxene are ~3 wt%. Primitive arc magmas have water contents ranging from 2 to 6 wt%, with a global average of ~4 wt% (Plank et al., 2013). The 1.7 to ~3 wt% water content of melts in equilibrium with the Wyoming pyroxenes overlap this range. We propose that this hydrous melt was associated with the Laramide flat slab, which extended >1000 km into the cratonic interior (Fig. 18) during the Cenozoic. Essentially, an extremely diffuse volcanic arc was formed during the Laramide, characterized by sparse and widely distributed volcanism far inboard of the

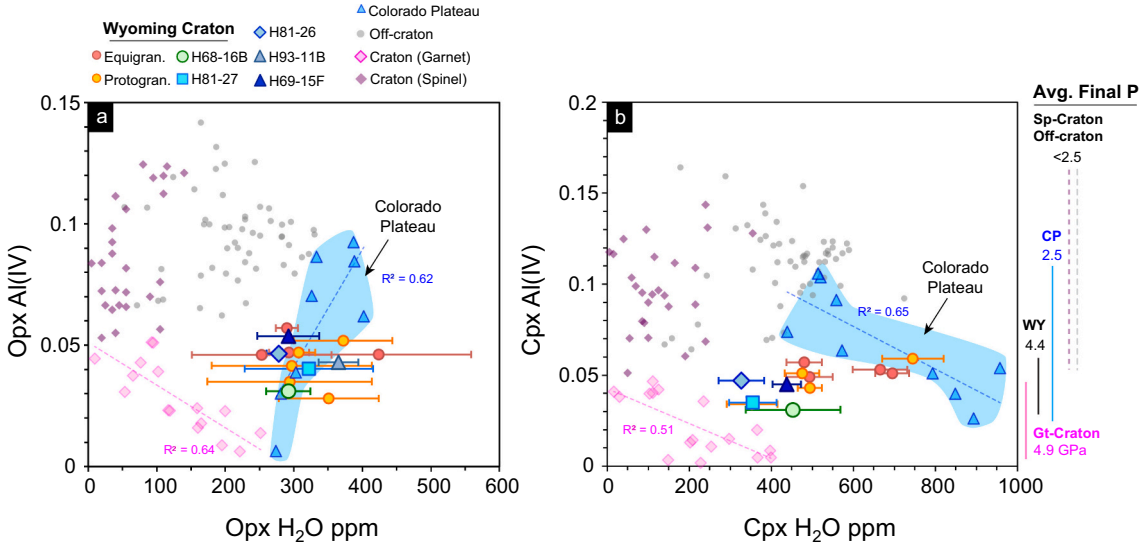


**Fig. 17.** (A) Orthopyroxene and (B) Clinopyroxene Al(IV) vs. orthopyroxene and clinopyroxene water contents. Pyroxene data and final PT from garnet-bearing cratonic peridotites, spinel cratonic peridotites, off-craton peridotites, and Colorado Plateau peridotites are from the compilation of Peslier et al. (2017).

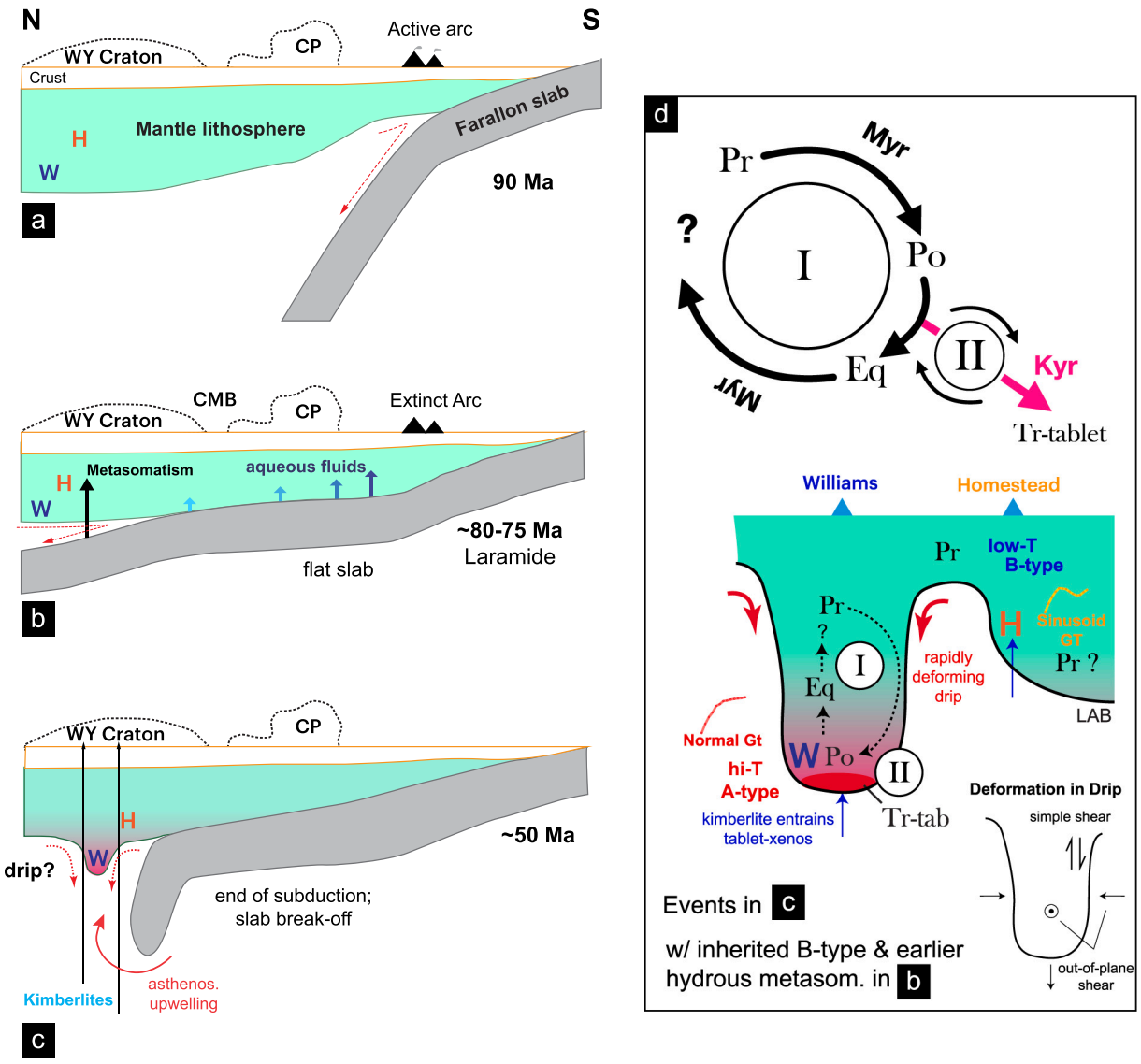


**Fig. 18.** Cartoon of proposed geodynamic scenario. A) Steep-angle subduction characterizes most of the Mesozoic Western US. Far inboard of the continental margin, subduction does not affect the Colorado Plateau or Wyoming Craton. B) During the Laramide Orogeny, low-angle subduction migrated magmatism inboard of the trench. Hydrous metasomatism caused by aqueous fluids coming off the Farallon slab infiltrated the Colorado Plateau mantle, and part of the Wyoming Craton mantle. Small amounts of hydrous melts may have formed and metasomatized the Wyoming Craton lithosphere, generating sinusoidal garnet REE patterns and B-type olivine fabric. C) The Laramide Orogeny ends around 50 Ma as the slab rolls back, exposing an asthenospheric window. Numerous kimberlites erupt through the Wyoming Craton at this time. The edge of the craton at Williams develops a lithospheric instability, heating up, deforming rapidly, and generating transitional-tablet xenoliths in a super-imposed deformation cycle II. D) The main peridotite deformation cycle is denoted by I; this cycle occurs over tectonic timescales. Homestead (H) xenoliths (protogranular, equigranular) represent the endpoints of the cycle. Williams (W) xenoliths represent the super-imposed cycle II associated with lithospheric instability. A cross-section view of the lithospheric drip is shown in D) based on C). The drip deforms rapidly under high-T, producing porphyroclastic to tablet textures at Williams, with A-type fabric and mostly normal garnet REE patterns. Kimberlite erupts shortly after tablets annealed, preserving the texture. Further away from the craton edge, Homestead mantle preserves relict Laramide B-type fabric and metasomatism (sinusoidal garnet REE). Although the Homestead xenoliths were also rapidly heated, they did not experience the high strain rates at Williams. The simplified "Deformation in Drip" sketch shows possible complex strain geometry in a drip that could explain discrepant bulk olivine CPO and MOA systematics. (See text for explanation). CP = Colorado Plateau, CMB = Colorado Mineral Belt, Gt = garnet, LAB = lithosphere-asthenosphere boundary.

continental margin (Coney and Reynolds, 1977). This is in contrast to the steep angle subduction characterizing much of the Cretaceous (Fig. 18a), which did not affect the Colorado Plateau and Wyoming Craton, but generated a narrow arc front along the continental margin. As the flat slab moved northeast from Arizona to Montana during the Laramide, it released fluids beneath the Colorado Plateau (Fig. 18b) – explaining the anomalously elevated water content of the sub-plateau mantle lithosphere (Li et al., 2008), as well as mineralization in the Colorado Mineral Belt. By the time the slab reached the vicinity of the Wyoming Craton, it was dehydrated, but still retained enough volatiles to impart hydrous metasomatism to the cratonic lithosphere. The flat slab appeared to have terminated somewhere beneath the Wyoming Craton, and part of it may have even "subcreted" onto its base (Humphreys et al., 2015) (Fig. 18b). At this time, the geometry of the slab may have permitted opening of a small mantle wedge generating small amounts of hydrous melt (e.g., Behr and Smith, 2016), which

subsequently infiltrated the base of the Wyoming mantle lithosphere and metasomatized it (Fig. 18b). Different melt/rock ratios throughout the lithosphere may explain the variation from normal garnet REE patterns to sinusoidal patterns. We note that, owing to the slow diffusivities of REE (even at high temperature), the hours to days timescale of kimberlite eruption cannot have produced the strongly sinusoidal patterns observed in the garnets in the Wyoming xenoliths (assuming the garnets had initial REE patterns characteristic of melt depletion). Thus, Laramide hydrous metasomatism is likely responsible for the observed pyroxene water contents and the trace element signatures in garnet and clinopyroxene.

### 8.3. Relationship between water content, REE patterns, CPO, and Wyoming Craton geodynamics

We observe the following broad correlation linking our geochemical and microstructural datasets across the Wyoming Craton xenolith suite: Cpx-recalculated olivine water content is highest (~40 to ~60 ppm) in Homestead xenoliths (Fig. 13a), which tend to have more extreme sinusoidal garnet REE patterns and B-type olivine fabric (Fig. 7, H00–12-1, H01-4A, H02-9E), and lowest (~20 to ~40 ppm) in Williams xenoliths (Fig. 13a), which tend to have more normal to mildly sinusoidal garnet REE patterns and A- and E-type olivine fabric. (Fig. 8, H93—11B, H81–26, W206, H69—15F). The equigranular xenoliths (Homestead samples H00–11-23, H00–11-16; Williams sample H68—16B) are either AG-type or B-type fabric (Figs. 7, 8) and generally have high cpx-recalculated olivine water content (Fig. 13a). However, Homestead equigranular xenoliths do not have the extremely sinusoidal garnet REE patterns shown by the protogranular samples (note, however, that only one Homestead equigranular xenolith was analyzed for garnet trace element composition). The coarse tabular equigranular Williams xenolith H68—16B also stands out from the other Williams xenoliths and the larger group of Wyoming xenoliths studied here. It is the only low-T (~900 °C) xenolith of the entire suite (Fig. 4). It also differs from the other analyzed Williams xenoliths in having extremely sinusoidal garnet REE, higher olivine water content, and a coarse tabular equigranular texture and is thus texturally similar to the Homestead equigranular group.

B-type olivine fabric is associated with elevated water contents (Karato et al., 2008) and AG-type fabric may be associated with metasomatism and melt infiltration (e.g., Chin et al., 2020a, 2020b). We propose that at Homestead, the observed protogranular and equigranular textures and predominantly B-type fabric reflect a largely "completed" hydrous deformation cycle – the intermediate porphyroclastic and transitional-tablet textures, if they were ever present, had largely evolved to equigranular, or, a major, high-stress deformation event did not occur in Homestead mantle. Assuming the CPO-water regime of Karato et al. (2008), Laramide hydrous deformation seems the most likely candidate to generate the B-type fabric at Homestead. Behr and Smith (2016) also found B-type and AG-type olivine fabrics in mantle xenoliths from the Colorado Plateau, thought to have been modified by the passage of the Farallon slab. The Williams xenolith H68—16B with AG-type fabric may represent a Laramide relict that escaped the major deformation event recorded by the porphyroclastic samples.

However, Fig. 13a shows that, despite variation in textural types, the average olivine water content across all Wyoming xenoliths is ~40 ppm, which is considerably higher than the ~20 ppm average (cpx-recalculated) for cratons worldwide (Chin and Palin, in review). Homestead xenoliths are slightly more hydrous (45 ppm on average) than Williams xenoliths (33 ppm). The former have "wet" B-type olivine fabric whereas the latter are dominated by "dry" A-type fabric to "wet" *E*-type fabric. Yet, the Williams A-type xenoliths contain a high abundance of "wet" E-type subgrains (Fig. 8). This suggests that both the protogranular and porphyroclastic groups may have started out with similar mantle water content. Thus, we propose a common, pre-Eocene mantle beneath the Wyoming Craton that experienced hydrous deformation.

Following Laramide hydrous deformation, slab rollback induced asthenospheric upwelling and elevated temperatures, which may have been focused more along the craton edges at Williams, overprinting the previously equilibrated Laramide hydrous fabric. Eocene rollback and kimberlite genesis perturbed the mantle at the edge of the craton, inducing small-scale convective instabilities (Cooper et al., 2020; Levander et al., 2011). This could have initiated lithospheric "drips" which would have removed the basal part of the Wyoming craton, resulting in a comparatively shallow (~180 km) present-day lithosphere-asthenosphere boundary (Fig. 4) (Hopper et al., 2014). Such high-strain (and therefore rapid), high-temperature deformation could be associated with a rapidly developing lithospheric instability, generating strongly porphyroclastic to mylonitic textures. Following the high strain event, the transitional-tablet texture developed. The steep array of final P-T's of the Wyoming Craton xenoliths (Fig. 4 and inset) support transient, rapid heating owing to faster equilibration of Fe—Mg thermometers compared to Al-based barometers (cf. Chin et al., 2012).

However, because the tablet-bearing xenoliths record high T's, such tablets would have been annealed if they had not been plucked by the kimberlite shortly after tablet growth. This is a rather fortuitous chain of events, but both the rapid timescales (~My) of Rayleigh-Taylor style drips (Lee, 2014) and the textural evidence of extreme strain localization (small grain sizes, fluidal textures) in the Williams transitional-tablet xenoliths facilitated preservation of this texture. We note that similar highly sheared textures were reported in Great Basin xenoliths by Dygert et al. (2019) and interpreted to represent extreme strain localization in a Rayleigh-Taylor type lithospheric instability.

### 8.4. Apparent discrepancy between bulk CPO and intragranular microstructure

We also discuss the apparent discrepancies between the observed bulk olivine fabric versus the intragranular microstructures as shown by the MOA distributions and SGB analyses (Figs. 7, 8, 12). In interpreting the CPO, we have assumed the deformation geometry is a simple shear kinematics (thus MOA distributions should correspond to scenario (1) in Fig. 9a). However, the deformation geometry in an evolving lithospheric drip may be more complex and involve both in-plane and out-of-plane components, producing more complicated MOA distributions shown in scenarios (2) and (3) in Fig. 9a. In Fig. 9b, we show a scenario where the bulk slip system inferred from the CPO and the analysis of MOA and SGB data contradict each other.

The relationship between bulk CPO, SGB, and MOA is also complicated by the prediction that CPO transitions involve significant strain. Texture inherited from a previous stage of deformation can have a strong effect on the CPO. The evolution of CPO from one deformation geometry to another has been shown to require a significant amount of strain ($\gamma \sim > 5$) to depict the latter deformation (e.g., Ismail et al., 2021, this volume; Boneh et al., 2015; Castelnau et al., 2009; Kumamoto et al., 2019; Skemer et al., 2011). In addition, it is unclear how pre-existing subgrain structures respond to shifts in strain geometry, and whether (and how) the newly formed dislocations interact with "inherited" SGBs since there is much less known about the way subgrain boundaries evolve with complex kinematics. However, subgrain boundaries slow recovery-rates under static conditions (e.g., White, 1977), which suggests that low-energy intragrain structures may also take a significant amount of strain and/or time to reflect the last deformation event.

Let us take the case of the high-T Williams xenoliths (Fig. 8). The most abundant SGB fabric type is E-type (Fig. 12), but the bulk fabric is A-type. If we assume that the pre-existing deformation conditions (i.e. during Laramide times), as discussed above, were hydrous, this would result in "wet" fabrics such as E-, C-, or B-type (i.e., those found at Homestead) and significant E-type SGBs. A subsequent rapid, hot deformation event (i.e. associated with an Eocene lithospheric drip) induced deformation dominated by the (010)[100] slip system (A-type fabric). The MOA of the high-T Williams xenoliths generally points to [001], but with increasing strain the strength of the maxima decreases

and a secondary (weaker) maxima parallel to [010] forms (e.g., H69—15F, Fig. 8). Perhaps the shift in the Williams high-T CPO and MOA reflects a transition from one texture to another with increasing strain, in which case the most deformed sample (H69—15F) may best reflect the most recent deformation event. At Homestead, which show no recent deformation microstructures, we observe the opposite – most of the subgrains are A-type, but the bulk fabric is B-type (Fig. 12).

An additional explanation for the complexity of the MOA, SGB, and CPO systematics could be that on average, cpx-recalculated olivine water contents fall near the ~40 ppm threshold for the transition from A- ("dry") to E- ("wet") fabrics (Karato et al., 2008). Thus, the diversity of SGBs observed could simply reflect deformation conditions that fall near this transition. The apparent discrepancy at Homestead ("dry", A-type SGBs, but "wet" B-type fabric) and at Williams ("wet", E-type SGBs, but "dry" A-type fabric) may then simply reflect SGBs forming at conditions near the A-E fabric transition.

Despite the apparent discrepancies in our integrated analysis of CPO, SGB, and MOA, the details of these analyses open up new hypotheses for fabric development in lithosphere undergoing deformation and metasomatism. We note that strongly deformed porphyroclastic and mylonitic peridotite xenoliths from the actively rifting lithosphere beneath East Africa also show bulk fabric and misorientation analyses indicating MOA distributions that do not relate neatly to the fabric type, and transitions from A- to E- to C-type fabrics within the same xenolith suite (Kaczmarek and Reddy, 2013). However, the study by Kaczmarek and Reddy (2013) did not analyze water content in olivine or pyroxenes. Future rock deformation experiments should address the role of non-simple shear deformation geometry and the behavior of pre-existing subgrain structures during shifts in fabric and strain.

### 8.5. *Implications for the general peridotite deformation cycle*

A major finding of our study is that the original transitional (transitional-tablet) texture of Mercier and Nicolas (1975) represents a rapid sub-cycle juxtaposed on the "background" peridotite deformation cycle (Fig. 2). In the case of the Wyoming Craton xenoliths, we speculate that the transitional-tablet texture reflects a transient heating, deformation, and brief annealing episode associated with developing lithospheric instability and kimberlite genesis (Boneh et al., 2021) (Fig. 18). Because kimberlite eruption and the heating/deformation/annealing that caused the tablets occurred closely spaced in time, the transitional tablet texture was captured and preserved by eruption. If such transitional-tablet xenoliths did not erupt, they would continue to evolve in the main peridotite deformation cycle, and their tablet grains would anneal to an equigranular (or tabular equigranular) texture, the "endpoint" of the deformation cycle (Fig. 1).

An additional consequence of the transitional tablet textural type continuing to evolve in the main deformation cycle is that the process that formed tablets – heating and annealing associated with the proto-kimberlite – may have resulted in water loss in olivine at high temperatures shortly before eruption or during eruption (Fig. 13a). Thus, the retention of un-erupted transitional-tablet mantle within the lithospheric mantle may act to restrengthen the cratonic lithosphere, aiding in its long-term preservation, and counter-acting earlier hydrous metasomatism. Re-cratonization is further helped by the drastic decrease in water solubility in olivine as temperature cools back to conditions along a cold cratonic geotherm (Zhao et al., 2004; cf. Chin et al., 2016). Repeated cycles of deformation, hydrous metasomatism, and kimberlite processes closely spaced in time (in the case of Wyoming, ~20 My between hydrous metasomatism+deformation and kimberlite) could reconcile the paradox of metasomatism and kimberlite genesis (processes which both enrich the depleted cratonic mantle in heat-producing elements and volatiles, as well as re-densify it due to metasomatic garnet crystallization) occurring beneath cold, depleted mantle keels. In other words, a delicate balance must be struck between enrichment and preservation if one is to invoke repeated episodes of hydration, metasomatism, and heating in cratons, because such processes make cratons inherently unstable.

However, the Wyoming Craton may be unique because of the deep impact of the Laramide Orogeny and ensuing tectonic plate reorganization, which clearly de-stabilized and thinned much of the original cratonic lithosphere. Not all kimberlites around the world are connected with low-angle subduction, and many kimberlites erupt within cratonic interiors apparently unrelated to any known tectonic event. Because erupted kimberlites represent a successful breaching of a proto-kimberlite, there are probably numerous un-erupted kimberlites throughout Earth history that initiated a secondary peridotite deformation cycle but failed to preserve it. These heating-deformation-annealing-dehydration deformation cycles would re-set the greater deformation cycle, but with a more complex "initial" texture.

## 9. Conclusion

Through a multi-faceted approach on a well-characterized suite of cratonic xenoliths from Montana, we integrate geochemical (volatiles, trace elements) and microstructural (CPO, subgrain microstructures) datasets to bring new insights to the classic peridotite deformation cycle of Mercier and Nicolas (1975). We show that across a craton, fabric varies from the protogranular texture in the interior, to highly deformed tectonite fabrics at the craton margin. Metasomatism involving hydrous fluids and silicate melts affected the cratonic lithosphere as a whole during Cenozoic flat slab subduction, but deformation is most localized at the craton margins. The peculiar tablet-bearing xenoliths (the Mercier and Nicolas' "transitional" texture) attest to a transient episode of heating, deformation, and annealing (a second peridotite deformation cycle) which is best explained as directly related to events surrounding the Eocene kimberlite magmatism and possibly related to an incipient lithospheric instability. This transitional-tablet texture appears to be common in cratonic xenolith suites worldwide, but has never received an adequate geologic explanation until now. It may be overlooked evidence of geodynamic instability. Collectively, our study provides a roadmap for xenolith studies moving forward for reconciling the complex inter-relationships between geochemical, microstructural, and regional tectonic and seismic constraints on the evolution of the deep continental lithosphere.

Supplementary data to this article can be found online at https://doi.org/10.1016/j.tecto.2021.229029.

## Declaration of Competing Interest

The authors declare that they have no known competing financial interests or personal relationships that could have appeared to influence the work reported in this paper.

## Acknowledgments

This work was supported by NSF EAR 1719208 to EJC and NSF EAR 1361487 to GH and AES. We thank the following individuals for instrumentation assistance: Soumen Mallick (LA ICP-MS), Joe Boesenberg (EPMA), Jianhua Wang (SIMS). We also thank Alain Vauchez and Andrea Tommasi for the invitation to submit to this special volume in honor of Adolphe Nicolas, and to Editor In Charge Philippe Agard and Guest Editor José Alberto Padrón-Navarta for their insightful critiques and efficient handling of the manuscript. We are grateful to reviewers Luiz Morales, Alex Lusk, and Zach Michels which greatly improved the manuscript.

## References


Arndt, N., Guitreau, M., Boullier, A.-M., Le Roex, A., Tommasi, A., Cordier, P., Sobolev, A., 2010. Olivine, and the origin of kimberlite. J. Petrol. 51, 573–602.

Aubaud, C., Hauri, E.H., Hirschmann, M.M., 2004. Hydrogen partition coefficients between nominally anhydrous minerals and basaltic melts. Geophys. Res. Lett. 31.

Ave'Lallemant, H.G., Carter, N.L., 1970. Syntectonic recrystallization of olivine and modes of flow in the upper mantle. Geol. Soc. Am. Bull. 81, 2203–2220.

Bachmann, F., Hielscher, R., Schaeben, H., 2011. Grain detection from 2d and 3d EBSD data: Specification of the MTEX algorithm. Ultramicroscopy 111, 1720–1733.

Baptiste, V., Tommasi, A.a., Demouchy, S., 2012. Deformation and hydration of the lithospheric mantle beneath the Kaapvaal craton, South Africa. Lithos 149, 31–50.

Basu, A.R., 1977. Textures, microstructures and deformation of ultramafic xenoliths from San Quintin, Baja California. Tectonophysics 43, 213–246.

Behr, W.M., Smith, D., 2016. Deformation in the mantle wedge associated with Laramide flat-slab subduction. Geochem. Geophys. Geosyst. 17, 2643–2660.

Bennett, V.C., DePaolo, D.J., 1987. Proterozoic crustal history of the western United States as determined by neodymium isotopic mapping. Geol. Soc. Am. Bull. 99, 674–685.

Bernard, R.E., Behr, W.M., Becker, T.W., Young, D.J., 2019. Relationships between olivine CPO and deformation parameters in naturally deformed rocks and implications for mantle seismic anisotropy. Geochem. Geophys. Geosyst. 20, 3469–3494.

Bird, P., 1984. Laramide crustal thickening event in the Rocky Mountain foreland and Great Plains. Tectonics 3, 741–758.

Bird, P., 1988. Formation of the Rocky Mountains, Western United States: a Continuum Computer Model. Science 239, 1501–1507.

Bleeker, W., 2003. The late Archean record: a puzzle in ca. 35 pieces. Lithos 71, 99–134.

Boneh, Y., Skemer, P., 2014. The effect of deformation history on the evolution of olivine CPO. Earth Planet. Sci. Lett. 406, 213–222.

Boneh, Y., Morales, L.F., Kaminski, E., Skemer, P., 2015. Modeling olivine CPO evolution with complex deformation histories: Implications for the interpretation of seismic anisotropy in the mantle. Geochem. Geophys. Geosyst. 16, 3436–3455.

Boneh, Y., Wallis, D., Hansen, L.N., Krawczynski, M.J., Skemer, P., 2017. Oriented grain growth and modification of 'frozen anisotropy'in the lithospheric mantle. Earth Planet. Sci. Lett. 474, 368–374.

Boneh, Y., Chin, E.J., Chilson-Parks, B.H., Saal, A.E., Hauri, E.H., Hearn Jr., C.B., Hirth, G., 2021. Microstructural shift due to post-deformation annealing in the upper mantle. Geochemistry, Geophysics, Geosystems 22, 1–19.

Boullier, A.M., Nicolas, A., 1975. Classification of textures and fabrics of peridotite xenoliths from South African kimberlites. In: Physics and Chemistry of the Earth. Elsevier, pp. 467–475.

Bunge, H., 1982. Texture Analysis in Materials Science. Butterworth's, London.

Bunge, H.-P., Grand, S.P., 2000. Mesozoic plate-motion history below the Northeast Pacific Ocean from seismic images of the subducted Farallon slab. Nature 405, 337–340.

Carlson, R.W., Irving, A.J., Schulze, D.J., Hearn Jr., B.C., 2004. Timing of Precambrian melt depletion and Phanerozoic refertilization events in the lithospheric mantle of the Wyoming Craton and adjacent Central Plains Orogen. Lithos 77, 453–472.

Carter, N.L., Tsenn, M.C., 1987. Flow properties of continental lithosphere. Tectonophysics 136, 27–63.

Castelnau, O., Blackman, D.K., Becker, T.W., 2009. Numerical simulations of texture development and associated rheological anisotropy in regions of complex mantle flow. Geophys. Res. Lett. 36 (12).

Chapman, A.D., 2017. The Pelona–Orocopia–Rand and related schists of southern California: a review of the best-known archive of shallow subduction on the planet. Int. Geol. Rev. 59, 664–701.

Chin and Palin, Water storage in cratonic mantle, in review.

Chin, E.J., Lee, C.-T.A., Luffi, P., Tice, M., 2012. Deep Lithospheric Thickening and Refertilization beneath Continental Arcs: Case Study of the P, T and Compositional Evolution of Peridotite Xenoliths from the Sierra Nevada, California. J. Petrol. 53, 477–511.

Chin, E.J., Soustelle, V., Hirth, G., Saal, A., Kruckenberg, S.C., Eiler, J., 2016. Microstructural and geochemical constraints on the evolution of deep arc lithosphere. Geochem. Geophys. Geosyst. 17, 2497–2521.

Chin, E.J., Soustelle, V., Liu, Y., 2020a. An SPO-induced CPO in composite mantle xenoliths correlated with increasing melt-rock interaction. Geochim. Cosmochim. Acta 278, 199–218.

Chin, E.J., Curran, S.T., Farmer, G.L., 2020b. Squeezing Water From a Stone: $H_2O$ In Nominally Anhydrous Minerals From Granulite Xenoliths and Deep, Hydrous Fractional Crystallization. Journal of Geophysical Research: Solid Earth 125 (e2020JB020416).

Christensen, N.I., Lundquist, S.M., 1982. Pyroxene orientation within the upper mantle. Geol. Soc. Am. Bull. 93, 279–288.

Coney, P.J., Reynolds, S.J., 1977. Cordilleran Benioff zones. Nature 270, 403–406.

Cooper, C., Farrington, R., Miller, M., 2020. On the destructive tendencies of cratons. Geology. 49 (2), 195–200.

Currie, C.A., Beaumont, C., 2011. Are diamond-bearing cretaceous kimberlites related to low-angle subduction beneath western North America? Earth Planet. Sci. Lett. 303, 59–70.

Dave, R., Li, A., 2016. Destruction of the Wyoming craton: Seismic evidence and geodynamic processes. Geology 44, 883–886.

Demouchy, S., Mackwell, S., 2006. Mechanisms of hydrogen incorporation and diffusion in iron-bearing olivine. Phys. Chem. Miner. 33, 347–355.

Demouchy, S., Jacobsen, S.D., Gaillard, F., Stern, C.R., 2006. Rapid magma ascent recorded by water diffusion profiles in mantle olivine. Geology 34, 429–432.

Dickinson, W.R., Snyder, W.S., 1978. Plate tectonics of the Laramide orogeny. In: Matthews, V. (Ed.), Laramide Folding Associated with Basement Block Faulting in the Western United States, Geological Society of America Memoir, vol. 151, pp. 355–366.

Downes, H., 1987. Relationship between geochemistry and textural type in spinel lherzolites, Massif Central and Languedoc, France. In: Nixon, P.H. (Ed.), Mantle Xenoliths. John Wiley & Sons Ltd., pp. 125–135

Drury, M., Roermund, H.V., 1989. Fluid assisted recrystallization in upper mantle peridotite xenoliths from kimberlites. J. Petrol. 30, 133–152.

Duke, G.I., Carlson, R.W., Frost, C.D., Hearn Jr., B., Eby, G.N., 2014. Continent-scale linearity of kimberlite–carbonatite magmatism, mid-continent North America. Earth Planet. Sci. Lett. 403, 1–14.

Dygert, N., Bernard, R.E., Behr, W.M., 2019. Great Basin mantle xenoliths record active lithospheric downwelling beneath Central Nevada. Geochem. Geophys. Geosyst. 20, 751–772.

Eggler, D.H., McCallum, M., Kirkley, M., 1987. Kimberlite-transported nodules from Colorado-Wyoming. A record of enrichment of shallow portions of an infertile lithosphere. Geological Society of America Special Paper 215, 77–90.

Embey-Isztin, A., 1984. Texture types and their relative frequencies in ultramafic and mafic xenoliths from Hungarian alkali basaltic rocks. Annls hist-nat Mus natn hung 76, 27–42.

Falus, G., Drury, M.R., van Roermund, H.L., Szabo, C., 2004. Magmatism-related localized deformation in the mantle: a case study. Contrib. Mineral. Petrol. 146, 493–505.

Farmer, G.L., Bowring, S.A., Williams, M.L., Christensen, N.I., Matzel, J.P., Stevens, L., 2005. Contrasting lower crustal evolution across an Archean-Proterozoic suture: Physical, chemical and geochronologic studies of lower crustal xenoliths in southern Wyoming and northern Colorado. In: Washington DC American Geophysical Union Geophysical Monograph Series, 154, pp. 139–162.

Farmer, G.L., Fritz, D.E., Glazner, A.F., 2020. Identifying Metasomatized Continental Lithospheric Mantle Involvement in Cenozoic Magmatism From Ta/Th Values, Southwestern North America. Geochemistry, Geophysics, Geosystems 21 (e2019GC008499).

Feeley, T., 2003. Origin and tectonic implications of across-strike geochemical variations in the Eocene Absaroka volcanic province, United States. The Journal of geology 111, 329–346.

Ferriss, E., Plank, T., Walker, D., 2016. Site-specific hydrogen diffusion rates during clinopyroxene dehydration. Contrib. Mineral. Petrol. 171, 1–24.

Field, M., Stiefenhofer, J., Robey, J., Kurszlaukis, S., 2008. Kimberlite-hosted diamond deposits of southern Africa: a review. Ore Geol. Rev. 34, 33–75.

Foley, S.F., 2008. Rejuvenation and erosion of the cratonic lithosphere. Nat. Geosci. 1, 503.

Francis, D., 1978. The implications of the compositional dependence of texture in spinel lherzolite xenoliths. The Journal of Geology 86, 473–485.

Hansen, L.N., Zhao, Y.-H., Zimmerman, M.E., Kohlstedt, D.L., 2014. Protracted fabric evolution in olivine: Implications for the relationship among strain, crystallographic fabric, and seismic anisotropy. Earth Planet. Sci. Lett. 387, 157–168.

Harte, B., 1977. Rock nomenclature with particular relation to deformation and recrystallisation textures in olivine-bearing xenoliths. The Journal of Geology 279–288.

Harte, B., Cox, K.G., Gurney, J.J., 1975. Petrography and geological history of upper mantle xenoliths from the Matsoku kimberlite pipe. Physics and Chemistry of the Earth 477–506.

Hauri, E.H., Gaetani, G.A., Green, T.H., 2006. Partitioning of water during melting of the Earth's upper mantle at H 2 O-undersaturated conditions. Earth Planet. Sci. Lett. 248, 715–734.

Hausel, W.D., 1998. Diamonds and Mantle Source Rocks in the Wyoming Craton with a Discussion of Other US Occurrences. Wyoming State Geological Survey.

Heaman, L.M., Phillips, D., Pearson, G., 2019. Dating kimberlites: methods and emplacement patterns through time. Elements: An International Magazine of Mineralogy, Geochemistry, and Petrology 15, 399–404.

Hearn, B.C., 2004. The Homestead kimberlite, Central Montana, USA: mineralogy, xenocrysts, and upper-mantle xenoliths. Lithos 77, 473–491.

Hearn, B.C., Boyd, F., 1975. Garnet peridotite xenoliths in a Montana, USA, kimberlite, Physics and Chemistry of the Earth. Elsevier, pp. 247–255.

Hearn, B., McGee, E., 1984. Garnet peridotites from Williams kimberlites, north-Central Montana, USA, Developments in Petrology. Elsevier, pp. 57–70.

Helmstaedt, H., Anderson, O.L., Gavasci, A.T., 1972. Petrofabric studies of eclogite, spinel websterite, and spinel lherzolite Xenoliths from kimberlite-bearing breccia pipes in southeastern Utah and northeastern Arizona. J. Geophys. Res. 77, 4350–4365.

Hielscher, R., Schaeben, H., 2008. A novel pole figure inversion method: specification of the MTEX algorithm. J. Appl. Crystallogr. 41, 1024–1037.

Higgie, K., Tommasi, A., 2012. Feedbacks between deformation and melt distribution in the crust-mantle transition zone of the Oman ophiolite. Earth Planet. Sci. Lett. 359, 61–72.

Higgie, K., Tommasi, A.a., 2014. Deformation in a partially molten mantle: Constraints from plagioclase lherzolites from Lanzo, western Alps. Tectonophysics 615, 167–181.

Hirschmann, M.M., 2000. Mantle solidus: Experimental constraints and the effects of peridotite composition. Geochem. Geophys. Geosyst. 1 (10).

Holtzman, B., Kohlstedt, D., Zimmerman, M., Heidelbach, F., Hiraga, T., Hustoft, J., 2003. Melt segregation and strain partitioning: implications for seismic anisotropy and mantle flow. Science 301, 1227–1230.

Hoover, W.F., Page, F.Z., Schulze, D.J., Kitajima, K., Valley, J.W., 2020. Massive fluid influx beneath the Colorado Plateau (USA) related to slab removal and diatreme

emplacement: evidence from oxygen isotope zoning in eclogite xenoliths. J. Petrol. 61, 1–18.
Hopper, E., Ford, H.A., Fischer, K.M., Lekic, V., Fouch, M.J., 2014. The lithosphere–asthenosphere boundary and the tectonic and magmatic history of the northwestern United States. Earth Planet. Sci. Lett. 402, 69–81.
Humphreys, E.D., Schmandt, B., Bezada, M.J., Perry-Houts, J., 2015. Recent craton growth by slab stacking beneath Wyoming. Earth Planet. Sci. Lett. 429, 170–180.
Ismail, W.B., Tommasi, A., Sanchez, M.A.L., Rutter, E.H., Barou, F., 2021. Deformation of upper mantle rocks with contrasting initial fabrics in axial extension. arXiv preprint.
Jacobson, C.E., Oyarzabal, F.R., Haxel, G.B., 1996. Subduction and exhumation of the Pelona-Orocopia-Rand schists, southern California. Geology 24, 547–550.
Jelsma, H.A., De Wit, M.J., Thiart, C., Dirks, P.H., Viola, G., Basson, I.J., Anckar, E., 2004. Preferential distribution along transcontinental corridors of kimberlites and related rocks of Southern Africa. S. Afr. J. Geol. 107, 301–324.
Jordan, T.H., 1981. Continents as a Chemical Boundary Layer. Philosophical transactions of the Royal Society of London. Series a. Mathematical and Physical Sciences 301, 359–373.
Jung, H., Karato, S.-I., 2001. Water-Induced fabric Transitions in Olivine. Science 293, 1460–1463.
Kaczmarek, M.-A., Reddy, S.M., 2013. Mantle deformation during rifting: Constraints from quantitative microstructural analysis of olivine from the East African Rift (Marsabit, Kenya). Tectonophysics 608, 1122–1137.
Karato, S.-I., 2010. Rheology of the deep upper mantle and its implications for the preservation of the continental roots: a review. Tectonophysics 481, 82–98.
Karato, S.-I., Jung, H., Katayama, I., Skemer, P., 2008. Geodynamic significance of seismic anisotropy of the upper mantle: new insights from laboratory studies. Annu. Rev. Earth Planet. Sci. 36, 59–95.
Katz, R.F., Spiegelman, M., Langmuir, C.H., 2003. A new parameterization of hydrous mantle melting. Geochem. Geophys. Geosyst. 4 (9).
Kumamoto, K.M., Warren, J.M., Hansen, L.N., 2019. Evolution of the Josephine Peridotite Shear zones: 2. Influences on Olivine Cpo Evolution. Journal of Geophysical Research: Solid Earth 124 (12), 12763–12781.
Lange, R.A., Carmichael, I.S.E., Hall, C.M., 2000. $^{40}Ar/^{39}Ar$ chronology of the Leucite Hills, Wyoming: eruption rates, erosion rates, and an evolving temperature structure of the underlying mantle. Earth Planet. Sci. Lett. 174, 329–340.
Le Roux, V., Tommasi, A., Vauchez, A., 2008. Feedback between melt percolation and deformation in an exhumed lithosphere, Aiasthenosphere boundary. Earth Planet. Sci. Lett. 274, 401–413.
Lee, C.T.A., 2014. 4.12 - Physics and Chemistry of Deep Continental Crust Recycling A2 - Holland, Heinrich D. In: Turekian, K.K. (Ed.), Treatise on Geochemistry, Second edition. Elsevier, Oxford, pp. 423–456.
Levander, A., Schmandt, B., Miller, M., Liu, K., Karlstrom, K., Crow, R., Lee, C.A., Humphreys, E., 2011. Continuing Colorado plateau uplift by delamination-style convective lithospheric downwelling. Nature 472, 461.
Li, Z.-X.A., Lee, C.-T.A., Peslier, A.H., Lenardic, A., Mackwell, S.J., 2008. Water contents in mantle xenoliths from the Colorado Plateau and vicinity: Implications for the mantle rheology and hydration-induced thinning of continental lithosphere. Journal of Geophysical Research: Solid Earth 113, B9.
Liu, L., Gurnis, M., Seton, M., Saleeby, J., Müller, R.D., Jackson, J.M., 2010. The role of oceanic plateau subduction in the Laramide orogeny. Nat. Geosci. 3, 353.
Long, M.D., Becker, T.W., 2010. Mantle dynamics and seismic anisotropy. Earth Planet. Sci. Lett. 297, 341–354.
Luffi, P., Saleeby, J.B., Lee, C.-T.A., Ducea, M.N., 2009. Lithospheric mantle duplex beneath the Central Mojave Desert revealed by xenoliths from Dish Hill, California. J. Geophys. Res. 114, B03202.
Mainprice, D., 2010. 2.16 Seismic anisotropy of the deep Earth from a mineral and rock physics perspective. Treatise on Geophysics 2, 437.
Mainprice, D., Tommasi, A.a., Couvy, H.l., Cordier, P., Frost, D.J., 2005. Pressure sensitivity of olivine slip systems and seismic anisotropy of Earth's upper mantle. Nature 433, 731–733.
Marvin, R., Hearn, B., Mehnert, H., Naeser, C., Zartman, R., Lindsey, D., 1980. Late Cretaceous-Paleocene-Eocene igneous activity in north-Central Montana. Isochron/West 29, 5–25.
McDonough, W.F., Sun, S.s., 1995. The composition of the Earth. Chem. Geol. 120, 223–253.
Menzies, M., Hawkesworth, C., 1986. Mantle Metasomatism.
Mercier, J.C.C., 1980. Magnitude of the continental lithospheric stresses inferred from rheomorphic petrology. Journal of Geophysical Research: Solid Earth 85, 6293–6303.
Mercier, J.-C.C., Nicolas, A., 1975. Textures and Fabrics of Upper-Mantle Peridotites as Illustrated by Xenoliths from Basalts. J. Petrol. 16, 454–487.
Mitchell, R.H., Bergman, S.C., Bergman, S.C., 1991. Petrology of Lamproites. Springer Science & Business Media.
Nicolas, A., Boudier, F., Boullier, A., 1973. Mechanisms of flow in naturally and experimentally deformed peridotites. Am. J. Sci. 273, 853–876.
Nicolas, A., Boudier, F., Bouchez, J., 1980. Interpretation of peridotite structures from ophiolitic and oceanic environments. Am. J. Sci. 280, 192–210.
O'Brien, H.E., Irving, A.J., McCallum, I., Thirlwall, M.F., 1995. Strontium, neodymium, and lead isotopic evidence for the interaction of post-suhduction asthenospheric potassic mafic magmas of the Highwood Mountains, Montana, USA, with ancient Wyoming craton lithospheric mantle. Geochim. Cosmochim. Acta 59, 4539–4556.
O'Leary, J.A., Gaetani, G.A., Hauri, E.H., 2010. The effect of tetrahedral Al3+ on the partitioning of water between clinopyroxene and silicate melt. Earth Planet. Sci. Lett. 297, 111–120.
Passchier, C.W., Trouw, R.A., 2005. Microtectonics. Springer Science & Business Media.
Peslier, A.H., Schönbächler, M., Busemann, H., Karato, S.-I., 2017. Water in the Earth's Interior: distribution and Origin. Space Sci. Rev. 212, 743–810.
Pike, J.N., Schwarzman, E., 1977. Classification of textures in ultramafic xenoliths. The Journal of Geology 85, 49–61.
Plank, T., Kelley, K.A., Zimmer, M.M., Hauri, E.H., Wallace, P.J., 2013. Why do mafic arc magmas contain~ 4wt% water on average? Earth Planet. Sci. Lett. 364, 168–179.
Precigout, J., Hirth, G., 2014. B-type olivine fabric induced by grain boundary sliding. Earth Planet. Sci. Lett. 395, 231–240.
Reynes, J., Jollands, M., Hermann, J., Ireland, T., 2018. Experimental constraints on hydrogen diffusion in garnet. Contrib. Mineral. Petrol. 173, 69.
Ross, J.V., 1983. The nature and rheology of the Cordilleran upper mantle of British Columbia: inferences from peridotite xenoliths. Tectonophysics 100, 321–357.
Saleeby, J., 2003. Segmentation of the Laramide Slab–evidence from the southern Sierra Nevada region. Geol. Soc. Am. Bull. 115, 655–668.
Seyler, M., Mattson, P.H., 1989. Petrology and thermal evolution of the Tinaquillo peridotite (Venezuela). Journal of Geophysical Research: Solid Earth 94, 7629–7660.
Silver, P.G., 1996. Seismic anisotropy beneath the continents: probing the depths of geology. Annu. Rev. Earth Planet. Sci. 24, 385–432.
Skemer, P., Hansen, L.N., 2016. Inferring upper-mantle flow from seismic anisotropy: an experimental perspective. Tectonophysics 668, 1–14.
Skemer, P., Katayama, I., Jiang, Z., Karato, S.I., 2005. The misorientation index: Development of a new method for calculating the strength of lattice-preferred orientation. Tectonophysics 411, 157–167.
Skemer, P., Sundberg, M., Hirth, G., Cooper, R., 2011. Torsion experiments on coarse-grained dunite: implications for microstructural evolution when diffusion creep is suppressed. Geol. Soc. Lond., Spec. Publ. 360 (1), 211–223.
Stalder, R., Skogby, H., 2003. Hydrogen diffusion in natural and synthetic orthopyroxene. Phys. Chem. Miner. 30, 12–19.
Stracke, K., Ferguson, J., Black, L., 1982. Structural setting of kimberlites in southeastern Australia. Kimberlites, Diatremes, and Diamonds: Their Geology, Petrology, and Geochemistry 15, 71–91.
Tappe, S., Smart, K., Torsvik, T., Massuyeau, M., de Wit, M., 2018. Geodynamics of kimberlites on a cooling Earth: Clues to plate tectonic evolution and deep volatile cycles. Earth Planet. Sci. Lett. 484, 1–14.
Tenner, T.J., Hirschmann, M.M., Withers, A.C., Hervig, R.L., 2009. Hydrogen partitioning between nominally anhydrous upper mantle minerals and melt between 3 and 5 GPa and applications to hydrous peridotite partial melting. Chem. Geol. 262, 42–56.
Tian, Z.-Z., Liu, J., Xia, Q.-K., Ingrin, J., Hao, Y.-T., Christophe, D., 2017. Water concentration profiles in natural mantle orthopyroxenes: a geochronometer for long annealing of xenoliths within magma. Geology 45, 87–90.
Tommasi, A.a., Tikoff, B., Vauchez, A., 1999. Upper mantle tectonics: three-dimensional deformation, olivine crystallographic fabrics and seismic properties. Earth Planet. Sci. Lett. 168, 173–186.
Tommasi, A., Mainprice, D., Canova, G., Chastel, Y., 2000. Viscoplastic self-consistent and equilibrium-based modeling of olivine lattice preferred orientations: Implications for the upper mantle seismic anisotropy. Journal of Geophysical Research: Solid Earth 105, 7893–7908.
Tommasi, A., Godard, M., Coromina, G., Dautria, J.-M., Barsczus, H., 2004. Seismic anisotropy and compositionally induced velocity anomalies in the lithosphere above mantle plumes: a petrological and microstructural study of mantle xenoliths from French Polynesia. Earth Planet. Sci. Lett. 227, 539–556.
Tommasi, A.a., Knoll, M., Vauchez, A., Signorelli, J.W., Thoraval, C.R., 2009. Structural reactivation in plate tectonics controlled by olivine crystal anisotropy. Nat. Geosci. 2, 423–427.
Warren, J.M., Hauri, E.H., 2014. Pyroxenes as tracers of mantle water variations. Journal of Geophysical Research: Solid Earth 119, 1851–1881.
Watterson, J., 1975. Mechanism for the persistence of tectonic lineaments. Nature 253, 520–522.
West, J.D., Fouch, M.J., Roth, J.B., Elkins-Tanton, L.T., 2009. Vertical mantle flow associated with a lithospheric drip beneath the Great Basin. Nat. Geosci. 2, 439–444.
White, S., 1977. Geological significance of recovery and recrystallization processes in quartz. Tectonophysics 39 (1–3), 143–170.
Whitmeyer, S.J., Karlstrom, K.E., 2007. Tectonic model for the Proterozoic growth of North America. Geosphere 3, 220–259.
Wu, F.-Y., Yang, J.-H., Xu, Y.-G., Wilde, S.A., Walker, R.J., 2019. Destruction of the North China craton in the Mesozoic. Annu. Rev. Earth Planet. Sci. 47, 173–195.
Xu, Y., Tang, W., Hui, H., Rudnick, R.L., Shang, S., Zhang, Z., 2019. Reconciling the discrepancy between the dehydration rates in mantle olivine and pyroxene during xenolith emplacement. Geochim. Cosmochim. Acta 267, 179–195.
Zhang, S., Karato, S.-I., 1995. Lattice preferred orientation of olivine aggregates deformed in simple shear. Nature 375, 774–777.
Zhao, Y.-H., Ginsberg, S., Kohlstedt, D., 2004. Solubility of hydrogen in olivine: dependence on temperature and iron content. Contrib. Mineral. Petrol. 147, 155–161.